Chapter 12
Irradiation Hardening and Deformation

Exposure of metals to irradiation results in an increase in the yield strength over a wide temperature range and is most pronounced at $T_{irr} < 0.3T_m$. Typical engineering stress–stress curves for fcc and bcc steelsare shown in Fig. 12.1. Note that for both crystal structures, in addition to increasing the yield strength, the ductility (measured either by total elongation or by uniform elongation) is reduced. Irradiation also increases the yield strength, σ_y much more than it does the ultimate tensile strength (σ_{UTS} or UTS) for both fcc and bcc metals. The approach of σ_y to σ_{UTS} results in a loss of ductility to the limit where $\sigma_y = \sigma_{UTS}$ and uniform elongation is zero. In bcc metals tested at low temperature, high fluences may even result in the disappearance of necking deformation with fracture occurring on the elastic line, rendering them totally brittle.

Irradiation-induced hardening in both fcc and bcc metals is caused by the production of the various defects discussed in Chaps. 3, and 7–9:

- Defect clusters
- Impurity–defect cluster complexes
- Dislocation loops (faulted or unfaulted, vacancy or interstitial type)
- Dislocation lines (dislocation loops that have unfaulted and joined the dislocation network of the original microstructure)
- Voids and bubbles
- Precipitates

This chapter will focus on the mechanisms of irradiation hardening in metals due to the various irradiation-produced defects. Before beginning a discussion of hardening, it is helpful to briefly review the basic elements of elasticity and plasticity theory [1], which will serve as a basis for understanding the effect of irradiation on hardening.

Additional material to this chapter can be downloaded from http://rmsbook2ed.engin.umich.edu/movies/

G.S. Was, *Fundamentals of Radiation Materials Science*,
DOI 10.1007/978-1-4939-3438-6_12

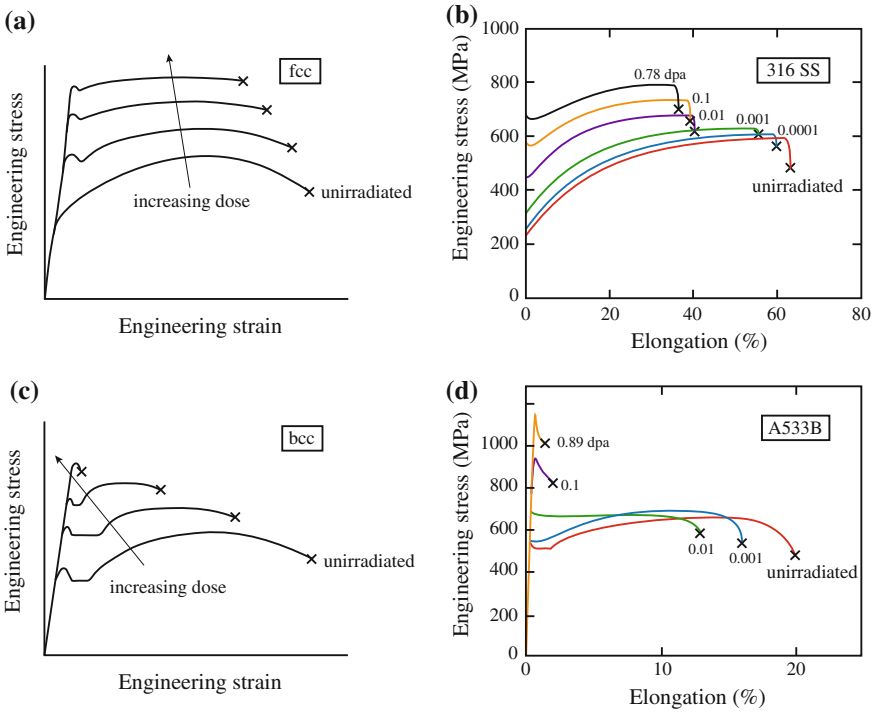

Fig. 12.1 Effect of irradiation on the stress–strain behavior (**a**) schematic and (**b**) example in an austenitic (fcc) stainless steel, and (**c**) schematic and (**d**) example in a ferritic (bcc) steel

12.1 Elastic and Plastic Deformation

12.1.1 Elasticity

In the elastic region, deformation is proportional to load, and the relation is known as Hooke's law:

$$\sigma = E\varepsilon, \tag{12.1}$$

where σ is stress, ε is strain, and E is the modulus of elasticity in tension or compression. While a tensile force in the x-direction produces extension along the x-axis, it also produces a contraction along the transverse y- and z-directions. The transverse strain is a constant fraction of the longitudinal strain:

$$\varepsilon_{yy} = \varepsilon_{zz} = -\nu\varepsilon_{xx} = \frac{-\nu\sigma_{xx}}{E}, \tag{12.2}$$

where v is the Poisson's ratio and has a value of 0.25 for perfectly isotropic elastic materials, but is approximately 0.33 for most metals. For a three-dimensional state of stress, the resulting strains are as follows:

Stress	x-Strain	y-Strain	z-Strain
σ_{xx}	$\varepsilon_{xx} = \frac{\sigma_{xx}}{E}$	$\varepsilon_{yy} = \frac{-v\sigma_{xx}}{E}$	$\varepsilon_{zz} = \frac{-v\sigma_{xx}}{E}$
σ_{yy}	$\varepsilon_{xx} = \frac{-v\sigma_{yy}}{E}$	$\varepsilon_{yy} = \frac{\sigma_{yy}}{E}$	$\varepsilon_{zz} = \frac{-v\sigma_{yy}}{E}$
σ_{zz}	$\varepsilon_{xx} = \frac{-v\sigma_{zz}}{E}$	$\varepsilon_{yy} = \frac{-v\sigma_{zz}}{E}$	$\varepsilon_{zz} = \frac{\sigma_{zz}}{E}$

Superposition of strain components yields:

$$\begin{aligned}
\varepsilon_{xx} &= \frac{1}{E}[\sigma_{xx} - v(\sigma_{yy} + \sigma_{zz})] \\
\varepsilon_{yy} &= \frac{1}{E}[\sigma_{yy} - v(\sigma_{xx} + \sigma_{zz})] \\
\varepsilon_{zz} &= \frac{1}{E}[\sigma_{zz} - v(\sigma_{xx} + \sigma_{yy})].
\end{aligned} \tag{12.3}$$

Adding the strain components gives the following:

$$\varepsilon_{xx} + \varepsilon_{yy} + \varepsilon_{zz} = \frac{1-2v}{E}(\sigma_{xx} + \sigma_{yy} + \sigma_{zz}), \tag{12.4}$$

and

$$\sigma_m = 1/3(\sigma_{xx} + \sigma_{yy} + \sigma_{zz}) \tag{12.5}$$

is the hydrostatic or mean stress, and

$$\Delta = \varepsilon_{xx} + \varepsilon_{yy} + \varepsilon_{zz} \tag{12.6}$$

is the volume strain. Shear stresses produce shear strains according to the following relations:

$$\varepsilon_{xy} = \frac{\sigma_{xy}}{\mu}, \quad \varepsilon_{yz} = \frac{\sigma_{yz}}{\mu}, \quad \varepsilon_{xz} = \frac{\sigma_{xz}}{\mu}, \tag{12.7}$$

where μ is the shear modulus.

The stress–strain relations for an isotropic solid involve three elastic constants, v, E, and μ, that are related as follows:

$$\mu = \frac{E}{2(1+v)}. \tag{12.8}$$

In a general anisotropic linear elastic solid, there are up to 21 independent elastic constants. Since the constants must obey various geometrical constraints for a given crystal structure, the number of independent elastic constants is reduced considerably in structures possessing a high degree of symmetry.

For small elastic strains, there is no coupling between the expressions for normal stress and strain and the equations for shear stress and shear strain and we can solve for stress in terms of strain. Writing Eq. (12.4) in terms of stress:

$$\sigma_{xx} + \sigma_{yy} + \sigma_{zz} = \frac{E}{1-2v}(\varepsilon_{xx} + \varepsilon_{yy} + \varepsilon_{zz}), \tag{12.9}$$

subtracting σ_{xx} from both sides of Eq. (12.9) and substituting for (σ_{yy} + σ_{zz}) into the first equation in Eq. (12.3) gives the following:

$$\varepsilon_{xx} = \frac{1+v}{E}\sigma_{xx} - \frac{v}{E}(\varepsilon_{xx} + \varepsilon_{yy} + \varepsilon_{zz}), \tag{12.10}$$

and solving for σ_{xx} gives the following:

$$\sigma_{xx} = \frac{E}{1+v}\varepsilon_{xx} + \frac{vE}{(1+v)(1-2v)}(\varepsilon_{xx} + \varepsilon_{yy} + \varepsilon_{zz}), \tag{12.11}$$

or in tensor notation:

$$\sigma_{ij} = \frac{E}{1+v}\varepsilon_{ij} + \frac{vE}{(1+v)(1-2v)}\varepsilon_{ij}\delta_{ij}, \tag{12.12}$$

where δ_{ij} is the Kronecker delta with values δ_{ij} = 1 for $i = j$, and δ_{ij} = 0 for $i \neq j$. (Note that the terms $\varepsilon_{ij}\delta_{ij}$ imply the use of Einstein notation.) Upon expansion, this expression yields three equations for normal stress and six equations for shear stress. Equation (12.12) is often written in briefer notation using the Lamé constant, defined as follows:

$$\lambda = \frac{vE}{(1+v)(1-2v)}. \tag{12.13}$$

Substituting for Eqs. (12.6), (12.8) and (12.13) for Δ, μ, and λ, respectively, into Eq. (12.11) gives the following:

$$\sigma_{xx} = 2\mu\varepsilon_{xx} + \lambda\Delta. \tag{12.14}$$

The stresses and strains can be broken into hydrostatic and deviatoric components. Hydrostatic stress involves only pure tension and compression while deviatoric stress represents the shear stresses in the total state of stress. The distortion is related to the stress deviator by:

$$\sigma'_{ij} = \frac{E}{1+v}\varepsilon'_{ij} = 2\mu\varepsilon'_{ij}, \tag{12.15}$$

while the relationship between hydrostatic stress and mean strain is given as:

$$\sigma_{ii} = \frac{E}{1-2v}\varepsilon_{ii} = 3K\varepsilon_{ii}, \tag{12.16}$$

where $K = \dfrac{E}{3(1-2v)}$ is the bulk modulus or volumetric modulus of elasticity. The bulk modulus is the ratio of the hydrostatic pressure to the dilatation that it produces:

$$K = \frac{\sigma_m}{\Delta} = \frac{-p}{\Delta} = \frac{1}{\beta}, \tag{12.17}$$

where $-p$ is the hydrostatic pressure and β is the compressibility of the solid. Note that the hydrostatic component of the stress tensor produces only elastic volume changes and does not cause plastic deformation. So the yield stress of a solid is independent of the hydrostatic stress. The stress deviator involves shear stress and is responsible for plastic deformation.

Two special cases of engineering importance are plane stress and plane strain. The plane stress state occurs when one of the principal stresses is zero, such as in a thin sheet loaded in the plane of the sheet (Fig. 12.2(a)) or an internally pressurized, thin-walled tube. In this case, the principal stresses are given as:

$$\begin{aligned} \sigma_1 &= \frac{E}{1-v^2}(\varepsilon_1 + v\varepsilon_2), \\ \sigma_2 &= \frac{E}{1-v^2}(\varepsilon_2 + v\varepsilon_1), \\ \sigma_3 &= 0. \end{aligned} \tag{12.18}$$

The plane strain state is one in which one of the principal strains is zero such as occurs when one dimension is much greater than the other two (Fig. 12.2(b)). In this case, we have $\varepsilon_3 = \dfrac{1}{E}[\sigma_3 - v(\sigma_1 + \sigma_2)]$, and combining with $\sigma_3 = v(\sigma_1 + \sigma_2)$ gives:

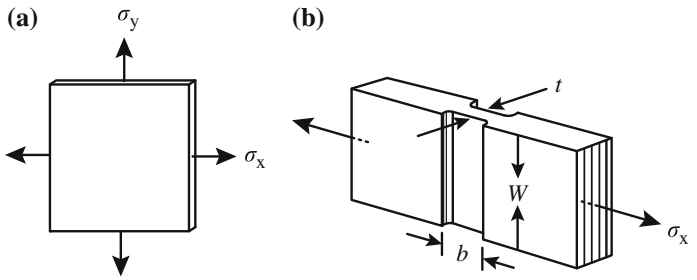

Fig. 12.2 Examples of (**a**) plane stress state and (**b**) plane strain state

$$\begin{aligned}\varepsilon_1 &= \frac{1}{E}[(1-\nu^2)\sigma_1 - \nu(1+\nu)\sigma_2],\\ \varepsilon_2 &= \frac{1}{E}[(1-\nu^2)\sigma_2 - \nu(1+\nu)\sigma_1],\\ \varepsilon_3 &= 0.\end{aligned} \tag{12.19}$$

Note that the expressions in Eqs. (12.18) and (12.19) are written in terms of principal stresses and principal strains, which act normal to the principal planes. Principal planes are those on which the maximum normal stresses act, and on which no shearing stresses act.

The strain energy, *U,* is the energy expended by the action of external forces in deforming an elastic body. The work performed during elastic deformation is stored as elastic energy and is recovered upon release of the applied forces. Energy is the product of force, *F,* through the distance, δ, over which it acts. In deformation of an elastic solid, the force and deformation increase linearly from zero to a value of $1/2F\delta$. This quantity is the area under the elastic portion of the stress–strain curve that was presented in Chap. 7 (Fig. 7.22). If we subject a cube to a tensile stress in the *x*-direction, then we can write an expression for the change in strain energy of the solid:

$$\begin{aligned}\mathrm{d}U &= 1/2F\,\mathrm{d}\delta\\ &= 1/2(\sigma_{xx}A)(\varepsilon_{xx}\mathrm{d}x)\\ &= 1/2(\sigma_{xx}\varepsilon_{xx})(A\mathrm{d}x).\end{aligned} \tag{12.20}$$

Since $A\ \mathrm{d}x$ is the volume increment, the strain energy per unit volume or strain energy density is:

$$\begin{aligned}u &= 1/2\sigma_{xx}\varepsilon_{xx}\\ &= 1/2\frac{\sigma_{xx}^2}{E}\\ &= 1/2\varepsilon_{xx}^2 E.\end{aligned} \tag{12.21}$$

For pure shear stress:

$$\begin{aligned}u &= 1/2\sigma_{xy}\varepsilon_{xy}\\ &= 1/2\frac{\sigma_{xy}^2}{\mu}\\ &= 1/2\varepsilon_{xy}^2\mu.\end{aligned} \tag{12.22}$$

Elastic strain energy for a three-dimensional stress state is obtained by superposition of Eqs. (12.21) and (12.22):

$$\begin{aligned} u &= 1/2(\sigma_{xx}\varepsilon_{xx} + \sigma_{yy}\varepsilon_{yy} + \sigma_{zz}\varepsilon_{zz} + \sigma_{xy}\varepsilon_{xy} + \sigma_{yz}\varepsilon_{yz} + \sigma_{xz}\varepsilon_{xz}) \\ &= 1/2\sigma_{ij}\varepsilon_{ij}. \end{aligned} \tag{12.23}$$

Substituting expressions for strains from Eqs. (12.3) and (12.7) gives the following:

$$\begin{aligned} u = \frac{1}{2E}\left(\sigma_{xx}^2 + \sigma_{yy}^2 + \sigma_{zz}^2\right) - \frac{v}{E}(\sigma_{xx}\sigma_{yy} + \sigma_{yy}\sigma_{zz} + \sigma_{xx}\sigma_{zz}) \\ + \frac{1}{2\mu}\left(\sigma_{xy}^2 + \sigma_{yz}^2 + \sigma_{xz}^2\right), \end{aligned} \tag{12.24}$$

and substituting Eq. (12.12) into Eq. (12.24) gives the following:

$$u = 1/2\lambda\,\Delta^2 + \mu(\varepsilon_{xx}^2 + \varepsilon_{yy}^2 + \varepsilon_{zz}^2) + 1/2\mu(\varepsilon_{xy}^2 + \varepsilon_{yz}^2 + \varepsilon_{xz}^2). \tag{12.25}$$

Note that the derivative of u with respect to any strain component gives the corresponding stress component:

$$\frac{\partial u}{\partial \varepsilon_{xx}} = \lambda\,\Delta + 2\mu\varepsilon_{xx} = \sigma_{xx} \quad \text{and} \quad \frac{\partial u}{\partial \sigma_{xx}} = \varepsilon_{xx}. \tag{12.26}$$

12.1.2 Plasticity

Elastic deformation depends only on the initial and final states of stress and strain, while plastic strain depends on the loading path by which the final state is achieved. The stress required to cause metal to flow plastically to any given strain describes the flow curve, which is given by the power law hardening relationship:

$$\sigma = K\varepsilon_{\mathrm{p}}^{n}, \tag{12.27}$$

where ε_{p} is the plastic strain, K is the stress at $\varepsilon_{\mathrm{p}} = 1.0$, and n is the strain hardening exponent. Note that $n = 0$ for perfectly plastic behavior and $n = 1$ for elastic behavior. Typically, n is between 0.1 and 0.5. The shape of the power law hardening curve for various values of n is shown in Fig. 12.3. The yield strength is easy to find in a tension test. We would like to develop mathematical relations for predicting the conditions under which plastic yielding begins when a material is subject to any possible combination of stresses. However, there is currently no way of calculating the relationship between the stress components to correlate yield in a three-dimensional state of stress with yield in uniaxial tension. All yielding criteria are empirical.

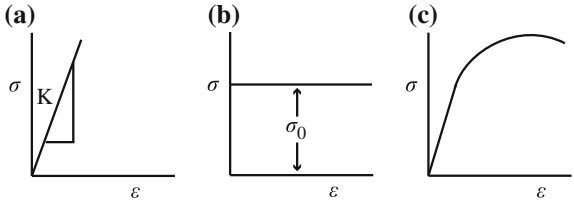

Fig. 12.3 Flow curves drawn from Eq. (12.27) for the cases (**a**) elastic behavior, $n = 1$, (**b**) perfectly plastic behavior, $n = 0$, (**c**) plastic behavior with intermediate value of n

Von Mises proposed that yielding will occur when the second invariant of the stress deviator (see for example [1]) exceeded some critical value, k^2, where:

$$k^2 = 1/6\left[(\sigma_1 - \sigma_2)^2 + (\sigma_2 - \sigma_3)^2 + (\sigma_3 - \sigma_1)^2\right]. \tag{12.28}$$

The value of k is determined by applying this expression to a uniaxial tension test in which $\sigma_1 = \sigma_y$, $\sigma_2 = \sigma_3 = 0$, (σ_y is the yield stress) giving:

$$\sigma_y^2 + \sigma_y^2 = 6k^2, \quad \text{or} \quad \sigma_y = \sqrt{3}k. \tag{12.29}$$

Substituting Eq. (12.29) into Eq. (12.28) gives the familiar form of the von Mises yield criterion:

$$\sigma_y = 1/\sqrt{2}\left[(\sigma_1 - \sigma_2)^2 + (\sigma_2 - \sigma_3)^2 + (\sigma_3 - \sigma_1)^2\right]^{1/2}, \tag{12.30}$$

and if shear stresses are present:

$$\sigma_y = 1/\sqrt{2}[(\sigma_{xx} - \sigma_{yy})^2 + (\sigma_{yy} - \sigma_{zz})^2 + (\sigma_{zz} - \sigma_{xx})^2 + 6(\sigma_{xy} + \sigma_{yz} + \sigma_{xz})]^{1/2}. \tag{12.31}$$

Yielding will occur when the differences in stresses on the right side of the equation exceed the yield stress in uniaxial tension, σ_y. For a pure shear stress state (as in a torsion test), the shear stress, σ_s, is related to the principal stresses by:

$$\sigma_1 = -\sigma_3 = \sigma_s, \quad \sigma_2 = 0, \tag{12.32}$$

and at yield:

$$\sigma_1^2 + \sigma_1^2 + 4\sigma_1^2 = 6k^2, \quad \text{and} \quad \sigma_1 = k, \tag{12.33}$$

so k is the yield stress in pure shear. The von Mises criterion predicts that the yield stress in torsion will be less than that in uniaxial tension by:

$$k = \frac{1}{\sqrt{3}}\sigma_y = 0.577\sigma_y. \tag{12.34}$$

Another criterion used for yielding due to a multiaxial stress state is the Tresca (or maximum shear stress) criterion, which says that yielding occurs when the maximum shear stress reaches the value of the shear stress in the uniaxial tension test:

$$\sigma_s^{max} = \frac{\sigma_1 - \sigma_3}{2}, \tag{12.35}$$

where σ_1 is the algebraically largest principal stress and σ_3 is the algebraically smallest principal stress. For uniaxial tension, $\sigma_1 = \sigma_y$, $\sigma_2 = \sigma_3 = 0$, and the shearing yield stress, σ_{sy}, is equal to $\sigma_y/2$, and (12.35) becomes:

$$\sigma_s^{max} = \frac{\sigma_1 - \sigma_3}{2} = \frac{\sigma_y}{2} = \sigma_{sy}, \tag{12.36}$$

so the maximum shear stress criterion is then given by:

$$\sigma_1 - \sigma_3 = \sigma_y. \tag{12.37}$$

For a pure shear stress state, $\sigma_1 = -\sigma_3 = k$, and $\sigma_2 = 0$; so the maximum shear stress criterion states that yielding will occur when:

$$\sigma_1 - \sigma_3 = 2k = \sigma_y, \quad \text{or} \quad k = \frac{\sigma_y}{2}. \tag{12.38}$$

The Tresca yield criterion has been observed to hold fairly well in alloys that exhibit a yield drop [2]. Alloys that yield by homogeneous plastic flow generally obey the von Mises criterion or deviate from it only slightly. In fact, in many real materials, the yield surface is "between" the Tresca and von Mises criteria [2].

12.1.3 Tension Test

The tension test is perhaps the best way to demonstrate the elastic and plastic behavior of metals. In a tension test, a specimen is subjected to a continually increasing uniaxial tensile force, while simultaneous observations are made of the elongation of the specimen. Data are plotted in a stress–strain diagram from load-elongation measurements, resulting in an engineering stress–engineering strain curve. The parameters used to describe the stress–strain curve are as follows:

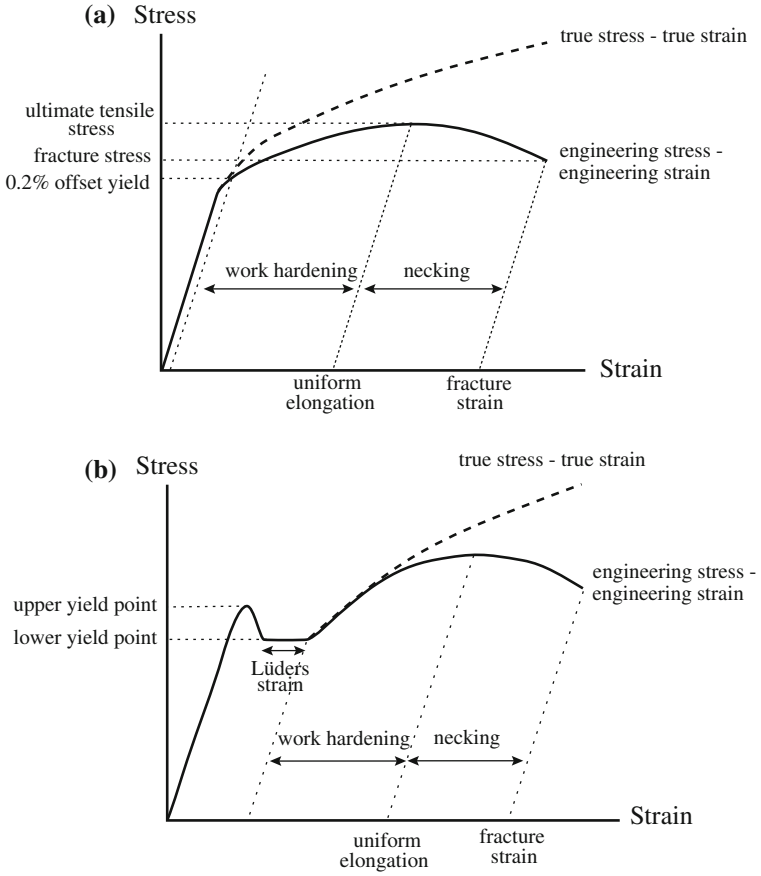

Fig. 12.4 Engineering stress–engineering strain and true stress–true strain curves resulting from a uniaxial tensile test and key parameters defining the curves for (**a**) fcc metals and (**b**) bcc metals

- Yield strength
- Tensile strength
- Fracture strength
- Uniform strain
- Fracture strain
- Reduction in area

Figure 12.4 illustrates the engineering stress–engineering strain curve and the parameters used to describe the behavior of the sample. The average longitudinal stress S is the load P divided by the *original* area, A_0:

$$S = \frac{P}{A_0}. \tag{12.39}$$

The average linear strain, e is the ratio of the change in length, δ to the original length, L_0:

$$e = \frac{\delta}{L_0} = \frac{\Delta L}{L_0} = \frac{L - L_0}{L_0}. \tag{12.40}$$

The engineering stress–engineering strain curve is not a true indication of the deformation characteristics of a material because it is based entirely on the original dimensions of the specimen that change continuously during a test.

The true stress, σ, and true strain, ε, are based on the instantaneous values of cross-sectional area and length and are given by:

$$\sigma = \frac{P}{A} = S\frac{A_0}{A}, \tag{12.41}$$

$$\begin{aligned} \varepsilon &= \int_{L_0}^{L_f} \frac{\mathrm{d}L}{L} \\ &= \ln\frac{L_f}{L_0} = \ln(e+1). \end{aligned} \tag{12.42}$$

While the true strain and engineering strain are close at small values of strain (<0.2), they diverge significantly at large values of strain. The relationship between true and engineering stress is determined by invoking conservation of volume:

$$\frac{A_0}{A} = \frac{L}{L_0} = e + 1, \quad \text{and} \quad \sigma = \frac{P}{A} = S(e+1). \tag{12.43}$$

Up to a certain limiting load, a solid will recover its original dimensions when the load is removed. The load beyond which the material no longer behaves elastically is the *elastic limit*. If the elastic limit is exceeded, the body will retain a permanent set upon removal of the load. The stress at which plasticity begins is called the *yield stress*, σ_y or YS. Various definitions exist for the yield stress but the commonly accepted one is the offset yield strength, determined by the stress corresponding to the intersection of the stress–strain curve and a line parallel to the elastic part of the curve and offset by a strain of 0.2 %. The yield strength is written as follows:

$$\sigma_y = \frac{P_{(\text{strain offset}=0.2\%)}}{A_0}. \tag{12.44}$$

The *tensile strength* or *ultimate tensile strength* (UTS) is the maximum load divided by the original cross-sectional area of the sample:

$$S_u = \frac{P_{\max}}{A_0}. \tag{12.45}$$

The true stress at maximum load is the true tensile strength and is given by the maximum load divided by the sample cross-sectional area at maximum load:

$$\sigma_{\mathrm{u}} = \frac{P_{\max}}{A_{\mathrm{u}}}, \quad \varepsilon_{\mathrm{u}} = \ln\frac{A_0}{A_{\mathrm{u}}}. \tag{12.46}$$

Eliminating $P_{\max}$ from Eqs. (12.45) and (12.46) gives:

$$\begin{aligned} \sigma_{\mathrm{u}} &= S_{\mathrm{u}}\frac{A_0}{A_{\mathrm{u}}} \\ &= S_{\mathrm{u}}\exp(\varepsilon_{\mathrm{u}}). \end{aligned} \tag{12.47}$$

The *fracture stress* is the stress at the point of failure and is given by:

$$\begin{aligned} S_{\mathrm{f}} &= \frac{P_{\mathrm{f}}}{A_0}, \quad e_{\mathrm{f}} = \frac{L_{\mathrm{f}} - L_0}{L_0} \\ \sigma_{\mathrm{f}} &= \frac{P_{\mathrm{f}}}{A_{\mathrm{f}}}, \quad \varepsilon_{\mathrm{f}} = \ln\frac{A_0}{A_{\mathrm{f}}}. \end{aligned} \tag{12.48}$$

Strain occurs uniformly in the gage section of the sample up to the UTS, which is when necking or localized deformation begins to occur. The true uniform strain, ε_{u}, is given by the strain at maximum load:

$$\varepsilon_{\mathrm{u}} = \ln\frac{A_0}{A_{\mathrm{u}}}. \tag{12.49}$$

The true fracture strain, ε_{f} is the true strain based on the original area and the area after fracture, A_{f}:

$$\varepsilon_{\mathrm{f}} = \ln\frac{A_0}{A_{\mathrm{f}}} = \ln\frac{1}{1 - RA}, \tag{12.50}$$

where RA is the reduction in area at fracture:

$$RA = \frac{A_0 - A_{\mathrm{f}}}{A_0}. \tag{12.51}$$

Finally, the local necking strain, ε_n, is the strain required to deform the specimen from the maximum load to fracture:

$$\varepsilon_n = \ln \frac{A_u}{A_f}. \tag{12.52}$$

A final quantity of importance in the tensile test is the onset of plastic instability, which occurs when the increase in stress due to the decreasing cross-sectional area becomes greater than the load-carrying ability of the metal. This necking or localized deformation begins at the point of maximum load and is defined by the condition that $dP = 0$:

$$\begin{aligned} P &= \sigma A \\ dP &= \sigma dA + A d\sigma = 0, \quad \text{and} \quad -\frac{dA}{A} = \frac{d\sigma}{\sigma} \end{aligned} \tag{12.53}$$

and from conservation of volume:

$$\frac{dL}{L} = -\frac{dA}{A} = d\varepsilon, \tag{12.54}$$

so that at the point of tensile instability:

$$\sigma = \frac{d\sigma}{d\varepsilon}. \tag{12.55}$$

That is, the point of necking at maximum load is obtained from the true stress–true strain curve by finding the point on the curve where the rate of strain hardening equals the stress. Referring back to the flow curve relation given in Eq. (12.27), the strain hardening exponent is defined by:

$$n = \frac{d \ln \sigma}{d \ln \varepsilon} = \frac{\varepsilon \, d\sigma}{\sigma \, d\varepsilon}, \quad \text{and} \quad \frac{d\sigma}{d\varepsilon} = n \frac{\sigma}{\varepsilon}. \tag{12.56}$$

Substituting Eq. (12.55) into Eq. (12.56) gives a simple expression for the true uniform strain:

$$\varepsilon_u = n. \tag{12.57}$$

That is, the true uniform strain is equal to the strain hardening exponent in the power law hardening expression, Eq. (12.27).

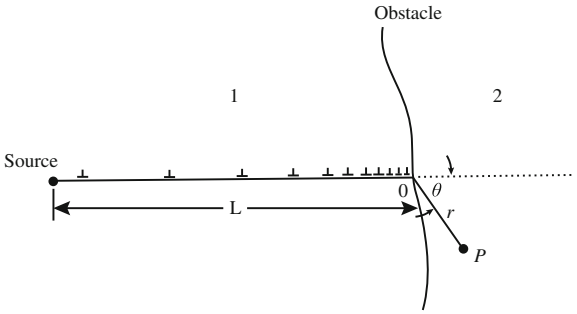

Fig. 12.5 Dislocation pileup at an obstacle in a solid

12.1.4 Yield Strength

The yield strength represents the onset of plasticity and hence is a key parameter in determining the mechanical behavior of metals. Yielding can be understood by examining the behavior of dislocations in a metal under stress. Dislocations formed by sources such as the Frank–Read source, frequently pile up on slip planes at barriers such as grain boundaries, precipitates, or sessile dislocations. The leading dislocation is acted on not only by the applied shear stress, but also by the interaction with other dislocations on the slip plane, leading to a high stress concentration on the lead dislocation in the pileup. The pileup of dislocations also exerts a back stress on dislocations further from the barrier, opposing their motion on the slip plane (Fig. 12.5). The high stress at the head of the pileup can initiate yielding on the other side of the barrier (or it may nucleate a crack at the barrier, see Chap. 14).

The number of dislocations in the pileup can be estimated by summing the x-direction forces between each dislocation in the pileup under the condition of mechanical equilibrium. The number of dislocations in a pileup of length L under a shear stress σ_s on the slip plane [3] is:

$$n = \frac{\pi(1-\nu)L\sigma_s}{\mu b}. \tag{12.58}$$

At large distances from the pileup, the array of n dislocations can be considered to act like a single dislocation with Burgers vector nb with a force equal to $nb\sigma_s$. A more complete analysis of the stress at the head of the pileup was made by Stroh [4] who showed that the tensile stress normal to the line OP in the neighboring grain is:

$$\sigma = \frac{3}{2}\left(\frac{L}{r}\right)^{1/2}\sigma_s \sin\theta\cos\theta/2. \tag{12.59}$$

The maximum value of σ occurs at $\theta = 70.5°$ and yields:

$$\sigma = \frac{2}{\sqrt{3}}\left(\frac{L}{r}\right)^{1/2}\sigma_s, \tag{12.60}$$

and the shear stress acting in the plane OP is given by:

$$\sigma_P = \beta\sigma_s\left(\frac{L}{r}\right)^{1/2}, \tag{12.61}$$

and β is a factor dependent on orientation with a value approximately equal to unity.

If the obstacle is a grain boundary, and the distance from the head of the pileup in grain 1 to the nearest dislocation source in grain 2 in Fig. 12.5 is r, and the length of the pileup, L, is taken to be equal to the grain diameter, d, then yielding will occur when the shear stress in the pileup, σ_s, reaches the shear stress to cause yielding, σ_{sy} or $\sigma_s = \sigma_{sy}$. If σ_{sd} is the stress required to nucleate slip in grain 2, then the shear stress causing yielding can be written as follows:

$$(\sigma_{sy} - \sigma_{si})\left(\frac{d}{r}\right)^{1/2} = \sigma_{sd}, \tag{12.62}$$

where σ_{si} is the friction stress, or the stress opposing dislocation motion in the slip plane. Equation (12.62) can be written in terms of the normal stress where $\sigma = M\sigma_s$ and M is the Taylor factor defined as the ratio of the axial stress to the resolved shear stress:

$$\begin{aligned}\sigma_y &= \sigma_i + M\sigma_{sd}\left(\frac{r}{d}\right)^{1/2} \\ &= \sigma_i + k_y d^{-1/2}.\end{aligned} \tag{12.63}$$

Equation (12.63) is the Hall–Petch equation, which describes the grain size dependence of the yield stress. Note that the yield strength increases with decreasing grain size. Yield behavior in metals is generally found to follow this relation for nominal grain sizes (few to hundreds of micrometers), but fails at very low grain sizes in the nanometer range.

12.2 Irradiation Hardening

Irradiation of a metal causes strengthening by *source hardening* and *friction hardening*. Source hardening is the increase in stress required to start a dislocation moving on its glide plane. The applied stress required to release a dislocation into its slip plane is called the *unpinning* or unlocking stress. Once moving, the

dislocation can be impeded by natural- or radiation-produced obstacles lying close to or in the slip plane. The resistance to motion caused by these obstacles is referred to as friction hardening. Both of these concepts will be discussed and then applied to describe the hardening resulting from each of the radiation-induced defects listed earlier. It should be noted, however, that the true distinction between source and friction hardening is unclear, as lattice hardening produces all the characteristics of the deformation that has been attributed to source hardening. The loss of distinction is due to the fact that the distance between defect clusters is less than the source length that would produce the observed critical shear stress. Therefore, the *source* cannot operate without interference from the lattice clusters [5]. Nevertheless, we will treat them separately in the following sections. Hardening mechanisms will first be discussed for single crystals containing an obstacle of a single type. The superposition of hardening from different origins in a single crystal will be treated next followed by an extension of theory to the polycrystalline solid.

12.2.1 Source Hardening

Source hardening is found in irradiated fcc, and both unirradiated and irradiated bcc metals. In unirradiated bcc metals, source hardening is manifested by the upper and lower yield points in the stress–strain curves (Fig. 12.4(b)) and is thought to be caused by the pinning or locking of dislocation lines by impurity atoms. Before a Frank–Read source can operate under an applied stress, the dislocation line must be unpinned from the impurities. This requires a larger stress than that to move the dislocation, causing a drop in the yield stress. Yield then continues at a constant *flow stress* (*Lüders* strain region) until the onset of work hardening which progresses in the same manner as in fcc metals.

Source hardening is found in irradiated fcc metals in which irradiation-produced defect clusters in the vicinity of Frank–Read sources raise the stress required to expand the loops and to permit source multiplication. Once the stress level is sufficient to release the source, the moving dislocations can destroy the small clusters and reduce the stress needed to continue the deformation.

In unirradiated fcc metals, the stress required to initiate dislocation motion is the unpinning stress of the Frank–Read sources in the metal and is given by Eq. (7.32a) as $\sigma_{\mathrm{FR}} = \frac{\mu b}{l}$, where μ is the shear modulus, b is the Burgers vector, and $l(=2R)$ is the distance between pinning points shown in Fig. 7.25. Note that the stress is inversely proportional to the distance between pinning points. The gradual onset of yielding characteristic in fcc metals is generally explained by a distribution of stresses required to operate the sources. At low applied stress, dislocation sources easiest to operate (with large separation between pinning points) begin to generate dislocations. As dislocations are generated and move through the lattice, they begin to pile up and exert a back stress on the dislocation source, ceasing its operation and hence

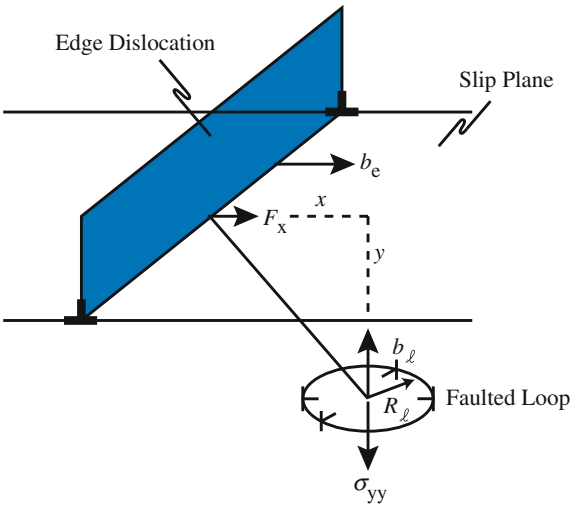

Fig. 12.6 Hardening by faulted loops caused by the interaction of stress fields between an edge dislocation moving on its slip plane located parallel to and displaced a distance y from the plane of the loop (after [3])

the plastic strain. With increasing applied stress, more dislocation sources are activated and dislocation multiplication increases.

Source hardening requires the dislocation line segment to bow out between the pinning points, which requires strong pinning. However, release of the dislocation will occur at lower values of applied stress if the dislocation segment is able to unlock itself before bowing occurs. That is, applied stresses below that required to operate a Frank–Read source are able to push the dislocation line segment past the pinning points. This process could occur, for example, if the pinning points consisted of small dislocation loops or defect clusters. The stress necessary to unlock a dislocation line segment from a small loop can be estimated using the analysis in [3].

Consider a group of edge character loops arranged in a row, each having Burgers vector b_ℓ, radius r, and spacing l, and are at a stand-off distance y from the straight edge dislocation of Burgers vector b_e, as shown in Fig. 12.6. Referring to the interaction between edge dislocations presented in Sect. 7.1.7, only the σ_{yy} term exerts a stress on the loop that acts to expand or contract it. The force on the loop due to the σ_{yy} component of stress from the straight edge dislocation is $2\pi r\sigma_{yy}b_\ell$, and the work to expand the loop is given as:

$$\begin{aligned} \frac{dW}{dr} &= 2\pi r\sigma_{yy}b_\ell \\ W &= \pi r^2\sigma_{yy}b_\ell. \end{aligned} \tag{12.64}$$

Substituting for the stress, σ_{yy}, given by Eq. (7.15), into Eq. (12.64) and differentiating with respect to x gives the force between the loop and the edge segment in the x-direction:

$$F_x = \frac{-\partial W}{\partial x} = -\frac{\mu b_\ell b_e r^2}{1-\nu}\frac{xy(3y^2 - x^2)}{(x^2+y^2)^3}. \tag{12.65}$$

Singh et al. [6] noted that the force is a maximum at an angle of about 40° between the distance vector and the glide plane of the dislocation and the value of the force can be written as a function of r/y:

$$F_x^{\max} \approx \frac{0.28\mu b^2}{(1-\nu)}\left(\frac{r}{y}\right)^2 \approx 0.4\mu b^2\left(\frac{r}{y}\right)^2, \tag{12.66}$$

for $\nu = 1/3$ and $b_\ell = b_e$. Given that $F = \sigma_s bl$, then:

$$\sigma_s = \frac{0.4\mu b}{l}\left(\frac{r}{y}\right)^2. \tag{12.67}$$

Singh suggests that $y = 1.5r$ is consistent with the observed microstructure, yielding a relation for the shear stress in terms of the loop spacing as:

$$\sigma_s = \frac{0.18\mu b}{l}. \tag{12.68}$$

Note that this value of shear stress is considerably less than that to initiate a Frank–Read source by bowing of the dislocation segment of $\sigma_{FR} = \frac{\mu b}{l}$.

Singh et al. also postulated that the unlocking process occurred by interaction between an edge segment and a network of loops that are no longer well separated, but have lost their individuality and act as a network. For this case, the yield stress can be estimated by the stress necessary to overcome the interaction between dislocation dipoles. This problem is treated in more detail in Chap. 13, in which the shear stress is provided in Eq. (13.23) as:

$$\sigma_s = \frac{\mu b}{8\pi(1-\nu)y} \approx \frac{0.06\mu b}{y}, \tag{12.69}$$

for $\nu = 1/3$.

12.2.2 Friction Hardening

Friction hardening refers to the stress required to sustain plastic deformation, which is often termed the flow stress, or friction stress. The forces responsible for resisting dislocation motion through a crystal lattice arise from the dislocation network and obstacles such as defect clusters, loops, precipitates, voids. These sources of

hardening are characterized as either long range or short range. Long-range stresses are caused by dislocation–dislocation interaction by virtue of their stress fields. Short-range stresses have their origin in the interaction between the moving dislocation and the discrete obstacles in the slip plane. The total applied shear stress necessary to overcome both long-range and short-range forces in order to move the dislocation is given as:

$$\sigma_{\mathrm{F}} = \sigma_{\mathrm{LR}} + \sigma_{\mathrm{SR}}, \tag{12.70}$$

where σ_{F} is the friction stress and the subscripts LR and SR represent long- and short-range contributions, respectively, and σ_{SR} is given by:

$$\sigma_{\mathrm{SR}} = \sigma_{\mathrm{ppt}} + \sigma_{\mathrm{void}} + \sigma_{\mathrm{loops}}, \tag{12.71}$$

where the terms on the right-hand side of the equality correspond to precipitates, voids, and loops, respectively.

Long-Range Stresses

Long-range forces arise from the repulsive interaction between a moving dislocation and components of the dislocation network of the solid. Dislocations on parallel glide planes exert forces on each other due to their stress fields, which constitute the long-range stress fields. Referring back to Eq. (7.50) describing the force between edge dislocations, the maximum force occurs at an angle $\theta = 0°$, which yields a value of:

$$F_x(0°) = F_{\mathrm{LR}} = \frac{\mu b^2}{2\pi(1-\nu)r}. \tag{12.72}$$

Taking ν = 1/3, and the distance between dislocations, r from Eq. (5.85) as $1/\sqrt{\pi\rho_{\mathrm{d}}}$, where ρ_{d} is the dislocation density gives:

$$F_{\mathrm{LR}} = \frac{\mu b^2\sqrt{\pi\rho_{\mathrm{d}}}}{4/3\pi} \approx \frac{\sqrt{\pi}\mu b^2\sqrt{\rho_{\mathrm{d}}}}{4} \approx \alpha\mu b^2\sqrt{\rho_{\mathrm{d}}}, \tag{12.73}$$

where α is a constant. The stress needed to overcome this force is $\sigma_{\mathrm{LR}} = F_{\mathrm{LR}}/b$, giving:

$$\sigma_{\mathrm{LR}} = \alpha\mu b\sqrt{\rho_{\mathrm{d}}}. \tag{12.74}$$

Note that if the long-range stress is equated to the unpinning stress given as the grain size-dependent term in Eq. (12.63), then the yield strength can be written as:

$$\sigma_{\mathrm{y}} = \sigma_{\mathrm{i}} + \alpha M\mu b\rho_{\mathrm{d}}^{1/2}. \tag{12.75}$$

Equation (12.75) actually represents a different way of obtaining the grain size dependence of the yield stress, since the dislocation density has been observed to vary with grain size, d as $\rho_d = 1/d$.

Short-Range Stresses

Short-range forces are due to the interaction between a moving dislocation and an obstacle that lies in its slip plane. Short-range forces arise only when the dislocation contacts the obstacle. Short-range forces can be classified into athermal and thermally activated interactions. An athermal stress interaction is independent of temperature and results in the dislocation bowing around the obstacle. In thermally activated processes, the dislocation will overcome the obstacle either by cutting through, or climbing over it. Both processes require the addition of energy through an increase in temperature. We will discuss dislocation bowing around the obstacle and obstacle cutting in this section, and the process of climb will be described in detail in Chap. 13 on creep.

The friction stress due to a dispersion of barriers depends on the average separation between the obstacles in the slip plane of the moving dislocation. Figure 12.7 shows a unit area of a slip plane that is intersected by portions of spherical objects of diameter d, which are randomly distributed throughout the solid at a concentration of N cm^{-3}. Any sphere that has its center within the slab of volume d centered on the slip plane intersects the slip plane. The number of obstacles in this volume element is Nd, which is also the number of intersections per unit area on the slip plane. The product of the number of intersections per unit area, Nd, and the square of the distance between obstacles, l^2, is unity, yielding the distance between obstacles:

$$l = (Nd)^{-1/2}. \tag{12.76}$$

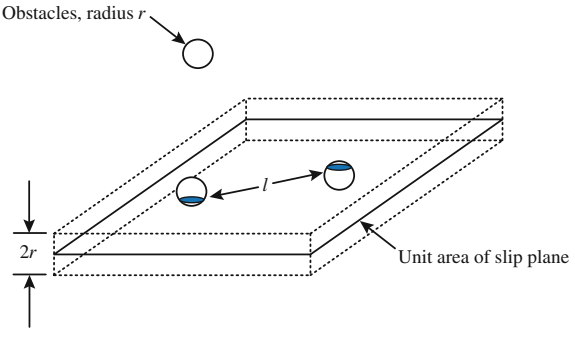

Fig. 12.7 Schematic showing the intersection of spherical obstacles of radius r and spacing l with a unit area of slip plane (after [3])

Precipitates

When a dislocation encounters an obstacle such as an incoherent precipitate, the short-range interaction occurs when it physically contacts the obstacle. For strong obstacles, an applied stress will cause the dislocation to bow out between the obstacles. Bowing will continue until adjacent segments touch and annihilate each other. This "pinch-off" process is exactly the same as occurs in a Frank–Read source. Following pinch-off, the dislocation is free to continue along its glide plane until it encounters the next obstacle and the process repeats itself. The obstacles are left with a dislocation loop surrounding them, which presents a stronger obstacle to the next dislocation that comes along (Fig. 12.8(a)). The short-range stress due to an array of obstacles of density N and size d is determined as follows. The line tension of an edge dislocation was given in Eq. (7.22) as $\Gamma \approx \frac{\mu b^2}{4\pi} \ln\left(\frac{R}{r_c}\right)$, where R is equated to the grain radius and r_c is the dislocation core radius and the dislocation

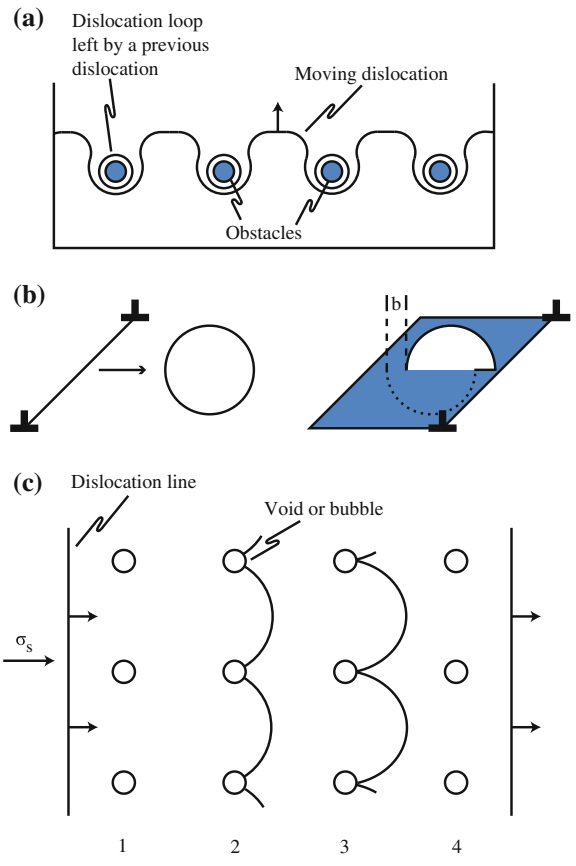

Fig. 12.8 (**a**) Dislocation bowing around hard obstacles such as precipitates. (**b**) Dislocation cutting of an obstacle such as a precipitate. (**c**) Dislocation interaction with voids

core energy is neglected. From Eq. (7.31), the shear stress is related to the line tension by $\sigma_s = \Gamma/bR$. Substituting for Γ from Eq. (7.22) and setting $R = l/2$ where l is the obstacle spacing gives:

$$\sigma_s \approx \frac{\mu b}{l}\frac{1}{2\pi}\ln\left(\frac{l}{2r_c}\right). \tag{12.77}$$

Substituting for l from Eq. (12.76) gives:

$$\sigma_s \approx \alpha\mu b\sqrt{Nd}, \tag{12.78}$$

where $\alpha \approx \frac{1}{2\pi}\ln\left(\frac{l}{2r_c}\right)$. The applied stress at yield, σ_y, is related to the resolved shear stress, σ_s, by the Taylor factor, M such that $\sigma_y = M\sigma_s$, and Eq. (12.77) can be written in terms of the applied stress as:

$$\sigma_y \approx \alpha M\mu b\sqrt{Nd}. \tag{12.79}$$

Stoller and Zinkle [7] have shown that M is actually an upper limit for the ratio of uniaxial yield strength to resolved shear strength and has the value of 3.06 for both fcc and bcc lattices. Equation (12.79) is generally written as:

$$\Delta\sigma_y = \alpha M\mu b\sqrt{Nd}, \tag{12.80}$$

where $\Delta\sigma_y$ represents the *increment* in the yield strength due to the obstacles of size d, number density N, and strength α. In fact, the term α represents the strength of the specific barrier in terms of the Orowan hardening model. A perfectly hard barrier would have a value of $\alpha = 1$. Hardening according to Eq. (12.80) is often termed *dispersed barrier* hardening after the original formulation of Seeger [8].

Dislocation bowing provides the greatest strengthening by obstacles. However, obstacle cutting can also provide strengthening. Obstacle cutting results in hardening by a variety of mechanisms, summarized by Dieter [1] as follows:

1. Shearing of the particle creates a step of width b on either side of the particle and the increase in surface area requires additional work be done to shear the particle.
2. If the particles are ordered structures, such as intermetallic compounds, then the shearing will also produce a new interface within the particle that will require extra energy.
3. Hardening also arises from the difference between the elastic moduli of the matrix and particle, which affects the line tension of the dislocation requiring additional stress to cut the particle.
4. Strengthening also occurs due to the difference in Peierls stress between the particle and matrix.

Figure 12.8(b) shows the result of a dislocation cutting an obstacle. The resulting obstacle is sheared and the top and bottom halves are displaced along the glide plane by an amount equal to the magnitude of the Burgers vector of the dislocation. Successive shearing of the obstacle on the same plane can result in complete separation of the two parts resulting in two smaller obstacles.

Molecular dynamic (MD) simulation of dislocation–obstacle interaction provides a means of visualizing complicated microstructural processes as shown in the following sections. It is important to note, however, that simulations are only as good as the interatomic potentials that define them and they may be influenced by other factors such as the size of the simulated volume and the strain rate. Hence, their value is largely in their qualitative description rather than as a strict quantitative interpretation.

Movies 12.1–12.3 (http://rmsbook2ed.engin.umich.edu/movies/) show molecular dynamic simulations of the interaction between a dissociated edge dislocation and a cobalt precipitate in copper as a function of precipitate size at a temperature of 10 K and under an applied stress of 100 MPa. The precipitate diameter in Movie 12.1 is 1.5 nm and it is sheared by both partials of the edge dislocation. Movies 12.2 and 12.3 are for 3 and 5 nm diameter precipitates, respectively, and show that while the first partial shears the precipitate, the trailing partial undergoes Orowan bowing and pinch-off, leaving a ring around the precipitate as shown in the schematic illustration in Fig. 12.8(a). Movie 12.4 shows the shearing of a 2-nm copper precipitate. The first part of the movie shows the behavior of the dislocation line in the shearing process, and the second part shows the shearing of the precipitate to result in an offset of the part of the precipitate above the slip plane relative to that below, as illustrated in Fig. 12.8(b).

For the case where hardening results from the difference in moduli between the precipitate and the matrix, such as for large vacancy clusters or copper-rich precipitates in ferritic pressure vessel steels, the Russell and Brown model [9] has been found to best describe hardening. They showed that the yield stress in shear is a function of the obstacle spacing in the slip plane, l, and the critical angle at which the dislocation can cut an obstacle, ϕ:

$$\begin{aligned} \sigma_{sy} &= 0.8\frac{\mu b}{l}\cos\frac{\phi}{2} \quad \text{for } \phi \leq 100^\circ \\ \sigma_{sy} &= 0.8\frac{\mu b}{l}\left(\cos\frac{\phi}{2}\right)^{3/2} \quad \text{for } \phi > 100^\circ \end{aligned} \tag{12.81}$$

and when $\phi = 0$, the stress is the Orowan stress. They showed that if a dislocation crosses an interface and has energy E_1 per unit length on one side and energy E_2 per unit length on the other, then the equilibrium of the dislocation requires that $E_1 \sin \theta_1 = E_2 \sin \theta_2$, where θ_1 and θ_2 are the angles between the dislocation and the normal to the interface. When the energy of the dislocation is lower in the precipitate than it is in the matrix ($E_1 < E_2$), then the angle ϕ has a minimum value

when the dislocation is about to break away, given by $\phi_{\min} = 2\sin^{-1}(E_1/E_2)$, and the strength from Eq. (12.81) is given by:

$$\begin{aligned} \sigma_{sy} &= 0.8\frac{\mu b}{l}\left[1-\frac{E_1^2}{E_2^2}\right]^{1/2} \quad \text{for } \sin^{-1}\frac{E_1}{E_2} < 50^\circ \\ \sigma_{sy} &= 0.8\frac{\mu b}{l}\left[1-\frac{E_1^2}{E_2^2}\right]^{3/4} \quad \text{for } \sin^{-1}\frac{E_1}{E_2} \geq 50^\circ, \end{aligned} \tag{12.82}$$

where:

$$\frac{E_1}{E_2} = \frac{E_1^\infty \log\frac{r}{r_c}}{E_2^\infty \log\frac{R}{r_c}} + \frac{\log\frac{R}{r}}{\log\frac{R}{r_c}}, \tag{12.83}$$

and E^∞ is the energy per unit length of dislocation in the infinite media, R is an outer cut-off radius (taken as half the distance to the next obstacle) and r_c is the dislocation core radius. The stresses in Eq. (12.82) depend inversely on the particle spacing, l, and therefore decrease as the particle radius increases (for constant volume fraction of precipitate). However, combining Eq. (12.83) with Eq. (12.82) yields a maximum in the relation between strength and precipitate size. For voids or for precipitates in pressure vessel steels, the maximum is at about $2r_c$ ($\sim$5a) or $\sim$1.5 nm.

Voids

Dislocations can also cut through voids, although the structure of the void is the same before and after the cut. Precipitates and voids are generally considered to be hard barriers with $\alpha \sim 1$. The only difference between passage of a mobile dislocation through precipitates and voids is that in the case of voids, the dislocation segments always meet the void surface at right angles and leave no dislocation ring after passage through the void (Fig. 12.8(c)). As described by Olander [3], the force to cut through a void is given by:

$$F = \frac{U_V}{R} = \sigma_s b l, \tag{12.84}$$

where U_V is the elastic strain energy in a volume of solid equal to the cavity, R is the radius of the cavity, and l is the void spacing on the slip plane. From Eq. (7.21), the elastic energy per unit volume for a screw dislocation is given as $W = \frac{\mu b^2}{8\pi^2 r^2}$. The elastic energy of the void–dislocation interaction energy can be approximated by the elastic energy in the volume of the void:

$$\begin{aligned} U_{\mathrm{v}} &= \int_{r_{\mathrm{c}}}^{R} 4\pi r^2 W \,\mathrm{d}r \\ &= 4\pi \int_{r_{\mathrm{c}}}^{R} \frac{\mu b^2}{8\pi^2} \mathrm{d}r \\ &= \frac{\mu b^2}{2\pi}(R - r_{\mathrm{c}}) \approx \frac{\mu b^2 R}{2\pi}. \end{aligned} \tag{12.85}$$

Substituting into Eq. (12.84) and solving for σ_{s} gives:

$$\sigma_{\mathrm{s}} = \frac{1}{2\pi}\frac{\mu b}{l}, \tag{12.86}$$

which is smaller than the Orowan stress, Eq. (7.32a) by a factor of $1/2\pi$ indicating that cutting of voids requires less energy than bowing around them. Written in the form of Eq. (12.80) gives:

$$\Delta\sigma_{\mathrm{y}} = \alpha M \mu b \sqrt{Nd}, \quad \alpha \approx 0.16 \tag{12.87}$$

A more complete treatment of dislocation–void interaction accounts for image stresses, dislocation self-interaction, and elastic anisotropy of the crystal. The image stress must be added to the dislocation stress in order to make the void surfaces traction free. Dislocation self-interaction refers to the dipole-like attractive forces between the dislocation branches terminating at a void, which can aid in pulling the branches together around the void, thus diminishing strengthening effects. Finally, elastic anisotropy of the crystal containing the void row must be accounted for in the dislocation stress field calculation. Inclusion of these factors in the calculation of the stress necessary for a dislocation to cut a void shows that the void is a very strong obstacle, approaching the Orowan stress value for impenetrable obstacles. A detailed treatment of these effects is given in [10].

The interaction between dislocations and voids is illustrated in Movies 12.5–12.7 (http://rmsbook2ed.engin.umich.edu/movies/). Movie 12.5 shows the interaction of leading and trailing partials of a dissociated edge dislocation with a 3 nm void in copper at 0 K. Note that the dislocation lines maintain a right angle with the void surface throughout the interaction. Movie 12.6 shows the shearing of a 1 nm void in iron by a dislocation and the resulting stress–strain behavior due to the dislocation–void interaction. In these three perspectives, the displacement of the top half of the void relative to the bottom half is evident. Finally, Movie 12.7 shows the repeated shearing by multiple dislocations of a 2.6 nm He bubble under an applied shear stress of 100 MPa. Note that the bubble appears to elongate in the direction of the applied stress, due to the offset of the half above the slip plane relative to that below, similar to that shown in Fig. 12.8(b).

Loops

The interaction between a mobile dislocation and a loop was described in Sect. 12.2.1 where it was shown that the stress in Eq. (12.68) is of the order $\sigma_s \sim \dfrac{0.2\mu b}{l}$ and for l given by Eq. (12.76) the stress becomes:

$$\sigma_s = 0.2\mu b\sqrt{Nd}, \tag{12.88}$$

which is well below the Orowan stress. Written in the form of Eq. (12.80), the yield strength increment due to loops is given as:

$$\Delta\sigma_y = \alpha M\mu b\sqrt{Nd}, \quad \text{with } \alpha \approx 0.2. \tag{12.89}$$

The types of interactions between dislocation lines and loops described in this chapter are illustrated in Movies 12.8–12.12 (http://rmsbook2ed.engin.umich.edu/movies/). In Movies 12.8 and 12.9, the interaction between the dislocation and the loop is through the stress fields. Movie 12.8 shows an edge dislocation in copper (edge on: red spheres are the partials), interacting with a 37 SIA perfect loop (green spheres) a distance 2 loop diameters from the dislocation. Both have Burgers vector 1/2[110]. Note that as the dislocation moves, the interacting strain fields drag the loop in the direction of the moving dislocation. Movie 12.9 shows an edge dislocation bypassing a 153 SIA Frank loop at 100 K under an applied stress of 300 MPa in copper. The blue spheres are atoms in the fcc crystal and the yellow spheres are atoms in the stacking fault. During the non-intersecting interaction, the Frank loop rotates to become a mobile perfect loop and glides to annihilation at the free surface.

Movies 12.10–12.12 illustrate interactions in which the dislocation contacts the loop. Movie 12.10 shows a dissociated screw dislocation shearing the same Frank loop under the same conditions as that shown in Movie 12.9. Note that the sheared loop is absorbed into the screw dislocation core. Movie 12.11 is another example of a screw dislocation interacting with a perfect loop (same Burgers vector) in which the loop is absorbed and then re-emitted a distance away from the original absorption point, and the dislocation cross slips onto a different glide plane. Movie 12.12 shows an edge dislocation interacting with and unfaulting a Frank loop (5 nm, 331 SIA) in iron at 300 K, resulting in near destruction of the loop.

Another type of faulted defect, the stacking-fault tetrahedron, described in Chap. 7, also interacts with dislocations and can contribute to hardening. Movie 12.13 shows the interaction of successive edge dislocations with a 153-vacancy SFT at 100 K under an applied stress of 100 MPa in copper. The SFT is sheared into a smaller SFT and a truncated base and subsequent interactions result in absorption of the truncated base into the dislocation. Movie 12.14 shows the details of the interaction between edge partials shown in Movie 12.13 but at a slower rate and with a 45-vacancy SFT.

Movies 12.15–12.17 show the interaction of a screw dislocation with an SFT in Cu. In Movie 12.15, the 45-vacancy SFT is sheared and in Movie 12.16, the 98-vacancy SFT is absorbed and then re-emitted. Movie 12.17 shows a 78-vacancy SFT being absorbed and re-emitted as a smaller SFT and a separate truncated base. A real-time movie of a dislocation–SFT interaction in copper was conducted on a sample under dynamic loading in the stage of a transmission electron microscope at room temperature, Movie 12.18. The SFTs were introduced by quenching the copper specimen in iced brine after a 2 h anneal at 1073 K. The weak-beam dark-field movie shows a dislocation being pinned by a stacking-fault tetrahedron. The result of the interaction is the formation of a perfect loop. Finally, Movies 12.19 and 12.20 show the interaction of a screw dislocation in copper with multiple defects: a 78-vacancy SFT and a perfect loop consisting of 61 interstitials in Movie 12.19 and 91 interstitials in Movie 12.20.

Effect of Temperature

As described in the preceding section, obstacle strength and density determine the velocity of dislocations in a polycrystal. If the Gibbs free energy of activation for cutting or bypassing an obstacle is $\Delta G(\sigma_s)$, then the mean velocity of a dislocation segment, $\bar{v}$, is given by [11]:

$$\bar{v} = \beta b v \exp\left(-\frac{\Delta G(\sigma_s)}{kT}\right), \tag{12.90}$$

where β is a dimensionless parameter, b is the magnitude of the Burgers vector, v is the ground frequency of the dislocation, and σ_s is the shear stress. The term $\Delta G(\sigma_s)$ is a function of the internal stress and the distribution of obstacles and for a regular array of obstacles, it can be expressed as:

$$\Delta G(\sigma_s) = \Delta F\left(1 - \frac{\sigma_s}{\sigma_s^0}\right), \tag{12.91}$$

where ΔF is the total free energy (activation energy) required to overcome the obstacle without aid from an external stress. The term σ_s^0 is the stress at which a dislocation can move through the obstacle with no help from thermal energy, or essentially, the flow stress at 0 K where $\Delta G = 0$.

Generalizing to a random array of obstacles [11], Eq. (12.91) becomes the following:

$$\Delta G(\sigma_s) = \Delta F\left[1 - \left(\frac{\sigma_s}{\sigma_s^0}\right)^p\right]^q, \tag{12.92}$$

Table 12.1 Strength of various obstacle types causing source and friction hardening in irradiated metals

Type of strengthening	Obstacle classification	Obstacle type	Stress increment	Value of α
Source		Loops	$\sigma_s = \frac{0.18\mu b}{l}$ isolated loops $\sigma_s \approx \frac{0.06\mu b}{y}$ loop network	
Friction	Long range	Dislocation network	$\sigma_{LR} = \alpha\mu b\sqrt{\rho d}$	<0.2
	Short range	Precipitates and voids	$\Delta\sigma_y = \alpha M\mu b\sqrt{Nd}$	1.0 bowing 0.3–0.5 cutting
		Dislocation loops		0.25–0.5
		Black dots		< 0.2

where $0 \le p \le 1$ and $1 \le q \le 2$, and where σ_s^0 is given phenomenologically by:

$$\frac{\sigma_s}{\sigma_s^0} = \left[1 - \left(\frac{T}{T_0}\right)^p\right]^q, \tag{12.93}$$

where reasonable limiting behavior is found with $p = 2/3$ and $q = 3/2$ [12]. Since the strain rate is proportional to the average dislocation velocity (see Sect. 13.1), the rate equation for discrete obstacle controlled plasticity is given by:

$$\dot{\varepsilon} = \dot{\varepsilon}_0 \exp\left\{-\frac{\Delta F}{kT}\left[1 - \left(\frac{\sigma_s}{\sigma_s^0}\right)^p\right]^q\right\}, \tag{12.94}$$

which captures both the stress and the temperature dependence of dislocation passage through a random array of obstacles.

Hardening due to long-range and short-range obstacles is summarized in Table 12.1 using Eq. (12.80) to describe short-range obstacles. Note that the values of α can vary by a significant amount depending on obstacle type. Much work has been done to determine the value of α experimentally, and column 5 in Table 12.1 gives the generally accepted values for α based on experimental work.

12.2.3 Superposition of Hardening Mechanisms

As discussed in Chaps. 7–9, the microstructure of an irradiated metal can be quite complicated. At very low dose, it consists of defect clusters and small loops. With increasing dose, the loop microstructure saturates at a particular number density and

loop size, and as loops unfault and become part of the dislocation line network, the dislocation density rises. At higher temperatures, voids and bubbles contribute to the microstructure, and irradiation-induced precipitation can also contribute. Each of these features presents a different type of obstacle to the moving dislocation. In order to assess the hardening of a true irradiated microstructure, we must have some way of accounting for obstacles of different types, sizes, and number densities. Below, we treat several special cases of various combinations of short-range and long-range obstacles as originally described by Bement [13].

Long-Range Stresses and Short-Range Obstacles

If long-range internal stresses exist in the lattice, as caused for example by groups of dislocations of predominantly the same sign of Burgers vector, and if in addition, dispersed barriers with a short-range interaction and an average distance, l_{SR} smaller than the average "wavelength" of the long-range stresses, are present, on average the effective stress available for pushing the dislocation over the short-range obstacles (σ_{SR}) is the difference between the applied stress σ_{a} and the stress σ_{LR} necessary for moving the dislocations through the long-range stress field:

$$\sigma_{\mathrm{a}} = \sigma_{\mathrm{LR}} + \sigma_{\mathrm{SR}}, \quad l_{\mathrm{SR}} < l_{\mathrm{LR}}. \tag{12.95}$$

Thus, the total stress is composed of the stress due to the two types of hardening as if each acted independently. Such is not the case if two types of short-range obstacles are present.

Two Types of Short-Range Obstacles

In an irradiated microstructure consisting of two types of short-range obstacles, the superposition depends sensitively on the strengths and relative concentrations of the two types of obstacles.

Two Strong Obstacles If both types of obstacles are strong such that dislocations interact by means of the Orowan mechanism, the moving dislocation cannot distinguish between them, and the sum of the area densities, *N,* of the two obstacles in the glide plane determines the effective obstacle distance:

$$l = \frac{1}{\sqrt{N_1 + N_2}}, \tag{12.96}$$

$$\text{and} \quad \frac{1}{l^2} = \frac{1}{l_1^2} + \frac{1}{l_2^2}, \tag{12.97}$$

$$\text{giving} \quad \sigma_{\mathrm{a}}^2 = \sigma_1^2 + \sigma_2^2, \tag{12.98}$$

where σ_1 and σ_2 are the critical (short-range) stresses of the obstacles of type 1 or 2 with average distances l_1 and l_2, respectively, would act separately. This root-sum-square (RSS) model was shown by Foreman and Makin [14] to apply for a population of obstacles with similar strengths. However, the behavior of the dislocation differs depending on the strength of the obstacle. Figure 12.9 shows the final configuration of a dislocation line just prior to yielding for obstacle strength, α, of 0.1, 0.5, and 0.8 [15]. If there are types of obstacles in the lattice which can be surmounted with the help of thermal activation and for which the forces (F_1 and F_2) are nearly the same, Eq. (12.98) holds for the same reasons given above.

Two Obstacles with Different Strengths There exist several subcases for combinations of weak and strong particles. Kocks [16] considered the case of many weak and a few strong obstacles giving the conditions:

$$F_1 \ll F_2 \quad \text{with} \quad l_1 \ll l_2. \tag{12.99}$$

If a dislocation segment bows out under the applied stress between two strong obstacles, it cuts through many weak ones in its path. The more it bows out the larger the angle becomes between neighboring branches of the dislocation at the weak obstacles and the smaller (at a given stress) the force is with which the dislocation is pressed against the weak obstacles. Simultaneously, the angle

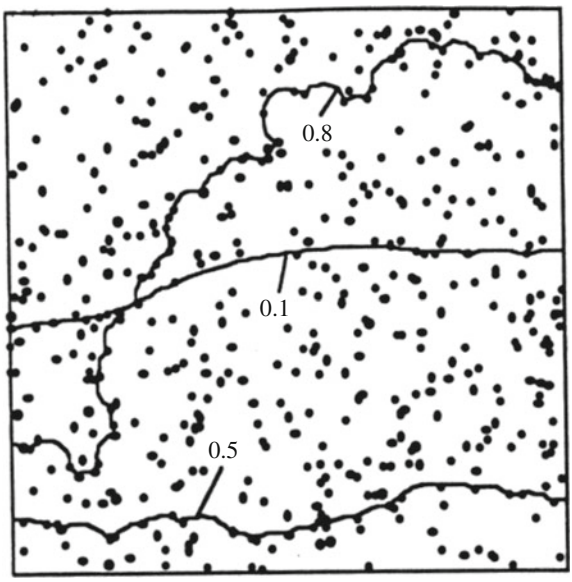

Fig. 12.9 Result of computer simulation of the shape of a dislocation line just prior to yielding for various fixed values of a (0.1, 0.5, 0.8) (after [15])

between the neighboring branches of the dislocation at the strong obstacles becomes smaller and the force acting on them increases (Fig. 12.10). The critical situation is reached when the dislocation can break through weak and strong obstacles simultaneously.

The applied stress required to push the dislocation through this critical configuration is given as:

$$\sigma_a = \sigma_1 + \sigma_2. \tag{12.100}$$

Movie 12.21 (http://rmsbook2ed.engin.umich.edu/movies/) is a real-time movie of dislocation–defect interaction during the straining of an irradiated copper sample. The sample was irradiated with 200 keV Kr^+ to a dose of about 10^{12} i/cm^2 at room temperature in the IVEM at Argonne National Laboratory. The defects consist predominantly of Frank loops with Burgers vector $a/3\langle 111\rangle$ and a smaller density (~ 10 %) of stacking-fault tetrahedra. As shown, the dislocation moves in a jerky manner with small segments breaking free from individual pining points and no observable defect absorption.

If no extreme condition exists as in Eq. (12.99), the thermally activated surmounting of the two types of obstacles must be treated in terms of so-called dependent processes. For such processes, the waiting time t_s (average time during which a dislocation is pressed against an obstacle of type s until it gets enough thermal energy to overcome it) enters the theoretical treatment additively, so that the time a dislocation needs for moving over a given area is proportional to $N_1t_1 + N_2t_2$. If $N_1t_1 \gg N_2t_2$, the effective flow stress is determined almost

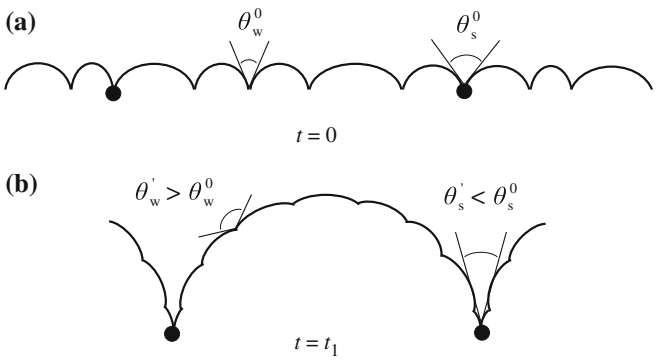

Fig. 12.10 Movement of a dislocation in an obstacle field consisting of many weak and a few strong obstacles (**a**) before application of a stress and (**b**) after the dislocation has moved past many of the weak barriers

exclusively by the obstacles of type 1; type 2 is "transparent" for the dislocation under the stress necessary to overcome type 1:

$$\sigma_a \approx \sigma_1 \quad \text{for } N_1 t_1 \gg N_2 t_2;\ \sigma_1 \gg \sigma_2 \tag{12.101a}$$

$$\sigma_a \approx \sigma_2 \quad \text{for } N_1 t_1 \ll N_2 t_2;\ \sigma_1 \ll \sigma_2. \tag{12.101b}$$

This means that if type 2 obstacles are added to a constant concentration of type 1 obstacles, Eq. (12.101a) holds for small concentration and Eq. (12.101b) for high concentrations of type 2 obstacles so that a transition occurs in the effective flow stress from σ_1 to σ_2. In extreme cases of very low or very high concentrations of type 2 obstacles, the stresses that the two types of obstacles would demand separately determine the effective flow stress.

In summary, the RSS superposition law, $\Delta\sigma_{yr} = \sqrt{\sum_i \left(\Delta\sigma_{yi}\right)^2}$ works well when obstacles have similar strengths, and the linear sum, or superposition law, $\Delta\sigma_{yl} = \sum_i \Delta\sigma_{yi}$ is better as the strengths become more dissimilar. Odette [16] has shown that hardening in a microstructure consisting of a wide range of obstacle strength is best fit by a combination of the root-square-sum and linear sum models, with the following weighting parameter, S:

$$\left(\Delta\sigma_y - \Delta\sigma_{yr}\right) = S\left(\Delta\sigma_{yl} - \Delta\sigma_{yr}\right) \tag{12.102}$$

and S can be related to the obstacle strengths by:

$$S \approx \alpha_s - 5\alpha_w + 3.3\alpha_s\alpha_w, \tag{12.103}$$

such that $S = 1$ for the linear sum law and $S = 0$ for the RSS law. According to Eq. (12.103), S decreases with increasing α_w (stronger weak obstacles) and decreasing α_s (weaker strong obstacles). The superposition rules for different hardening mechanisms are summarized in Table 12.2.

Using Eqs. (12.80) and (12.75), observed trends in the dose and temperature dependence for ρ_d and $\sqrt{Nd}$, and the obstacle strengths ($\alpha_{voids} = 1.0$) listed in Table 12.1, Lucas [17] estimated the hardening as a function of dose for three temperatures, as shown in Fig. 12.11. While these are only predictions, they serve to illustrate the relative contributions to hardening of the various microstructure features. In stainless steels, low-temperature (100 °C) hardening is dominated by black dot damage and small loops at low doses and the network density at higher doses. Above about 400 °C, voids and bubbles begin to make a contribution to the hardening. Intermediate to these temperatures, hardening is a maximum (near 300 °C) due to the combination of black dots, loops, and He bubbles. At lower doses, voids and loops contribute the majority of hardening, but at higher doses, the dislocation microstructure and voids become the major source of hardening [18]. These predictions differ somewhat from LWR data at ~300 °C [19] and even up to 400 °C [20, 21] in that the peak in hardness is not observed. This is likely due to the stability

Table 12.2 Superposition rules for hardening

I. Long-range stresses and short-range obstacles
$\sigma_a = \sigma_{LR} + \sigma_{SR}$
II. Two types of short-range obstacles
A. Both types strong
$l = \dfrac{l}{\sqrt{N_1 + N_2}}$
$\sigma_a^2 = \sigma_1^2 + \sigma_2^2$
B. Many weak and few strong
$F_1 < F_2;$ with $l_1 < l_2$
$\sigma_a = \sigma_1 + \sigma_2$
C. Thermally activated motion over barrier
$\sigma_a \approx \sigma_1$ for $N_1 t_1 \gg N_2 t_2; \tau_1 \gg \tau_2$
$\sigma_a \approx \sigma_1$ for $N_1 t_1 \ll N_2 t_2; \tau_1 \ll \tau_2$
III. Wide range of obstacle strength
$(\sigma_y - \sigma_{yr}) = S(\sigma_{yl} - \sigma_{yr})$
$S \approx \alpha_s - 5\alpha_w + 3.3\alpha_s\alpha_w$

of the loop microstructure to high doses at temperatures below 400 °C. At high temperature (600 °C), hardening is dominated by network dislocations. The contribution from voids can be significant at very high doses.

12.2.4 Hardening in Polycrystals

Up to this point, we have considered hardening only in single crystals and have not accounted for the effect of grain boundaries in polycrystalline metals. In polycrystals [13], the flow stress is increased by the influence of the different grain orientations and of the grain boundaries. As described by Eq. (12.63), the *tensile* yield stress depends on the grain size d according to the Hall–Petch relation given by $\sigma_y = \sigma_i + k_y d^{-1/2}$, where σ_i is the friction stress and k_y is the unpinning stress. The term k_y is based on the premise that a slip band is a stress concentration and that plastic flow between grains, and therefore, throughout the polycrystalline solid occurs when the stress concentration due to a dislocation pileup at a boundary is sufficient to activate a dislocation source in the neighboring grain. In the case of iron, steel, and molybdenum, the effect of irradiation on the Hall–Petch relationship is to increase the friction stress σ_i, with little effect on k_y for small grain sizes. For larger grain sizes, samples undergo a greater increase in yield strength which reduces k_y to almost zero (Fig. 12.12).

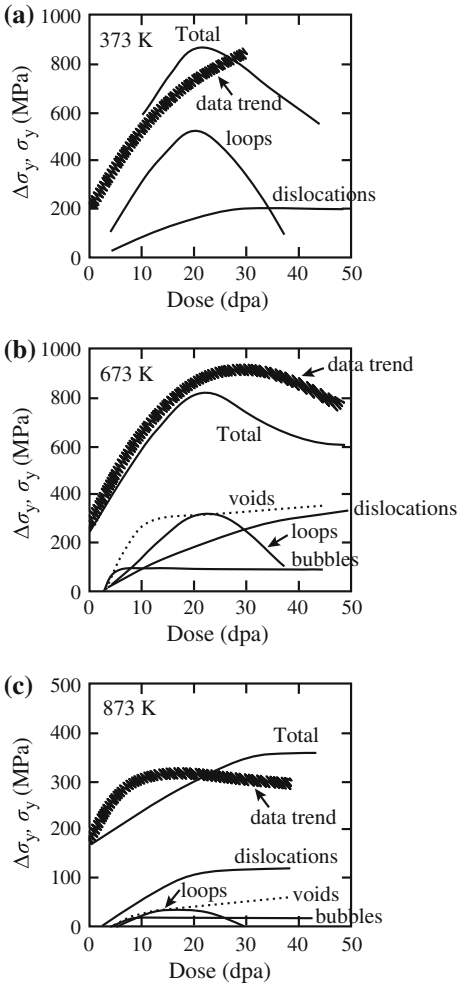

Fig. 12.11 Comparison of model predictions of the contribution to hardening from various microstructure features to data trends at (**a**) 100 °C, (**b**) 400 °C, and (**c**) 600 °C (after [17])

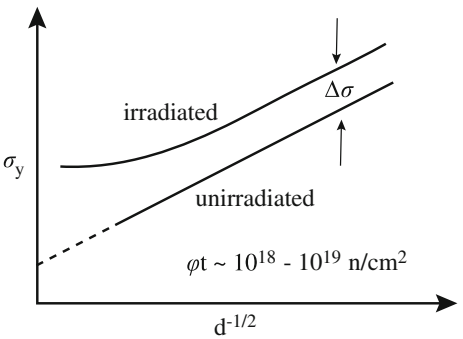

Fig. 12.12 Effects of irradiation on the Hall–Petch relationship for ferritic steel (after [13])

The dislocation density in a solid undergoing plastic deformation increases linearly with strain, ε according to:

$$\rho = \rho_0 + A\varepsilon, \tag{12.104}$$

and

$$A = \beta/d, \tag{12.105}$$

where β is a constant and d is the grain diameter. Recall from Eq. (12.75) that the yield strength is related to the dislocation density by: $\sigma_y = \sigma_i + \mu b \rho_d^{1/2}$, and using Eqs. (12.104) and (12.105) and assuming that $\rho_0 \ll A\varepsilon$, the yield strength can be written as:

$$\sigma_y = \sigma_i + \mu b \left(\frac{\beta\varepsilon}{d}\right)^{1/2}, \tag{12.106}$$

which is equivalent to the Hall–Petch equation with:

$$k_y = \mu b(\beta\varepsilon)^{1/2}. \tag{12.107}$$

In this work hardening model, β is a measure of work hardenability due to dislocation channeling. As β approaches zero in irradiated material because of loss of strain hardenability due to dislocation channeling, the term $\beta\varepsilon/d$ becomes very small and k_y approaches zero.

Data from a low alloy Fe–Mn–C steel was used to chronicle the development of radiation hardening using the Hall–Petch parameters, as well as the strength coefficient K and the strain hardening exponent, n from the power law hardening equation given in Eq. (12.27). Four stages of radiation hardening of a Fe–Cr–Mn steel with progressively increasing dose are shown in Fig. 12.13. Stage A occurs for very low dose (10^{15}–10^{16} n/cm^2) and involves an increase in k_y with negligible increase in stress σ_i, and no change in n and K. The result is an increase in the upper yield point and the Lüder's strain. Stage B occurs around 10^{18} n/cm^2 and represents an increase in σ_i but little change in k_y. In this stage, both n and K decrease, resulting in a reduced slope of the stress–strain curve and an increase in the Lüder's strain. Stage C appears at fluences of about 3×10^{18} n/cm^2 and is characterized by a continued increase in σ_i and a decrease in k_y. The strain hardening exponent, n, continues to decrease but K increases slightly, resulting in a small change in the slope of the stress–strain curve and a small decrease in Lüder's strain. In stage D, σ_i continues to increase and k_y falls nearly to zero. Also both n and K decrease, resulting in a further decrease in the slope of the stress–strain curve and the near disappearance of Lüder's strain. Although this description of the effects of irradiation on stress–strain behavior is specific to the iron alloy system, the changes in the parameters σ_i and k_y are consistent with the current understanding of barrier–hardening interactions, dislocation channeling, and grain size effects, and highlight

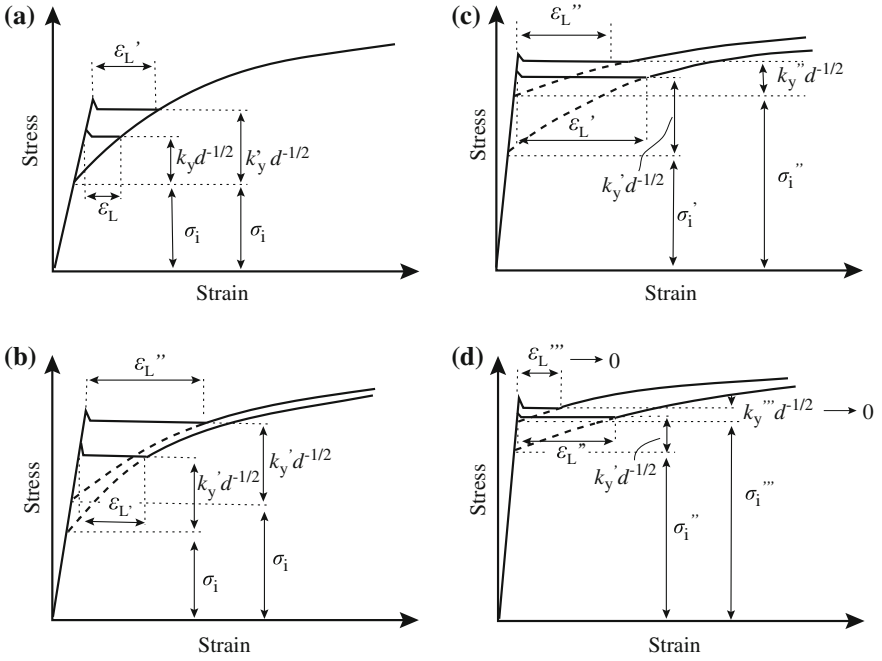

Fig. 12.13 Changes in the stress–strain curves for Fe–Cr–Mn steel irradiated at 80–100 °C to neutron doses of (**a**) 10^{16} n/cm^2, (**b**) 10^{18} n/cm^2, (**c**) 3×10^{18} n/cm^2, (**d**) $>5 \times 10^{18}$ n/cm^2 (after [13])

the changing nature of the fluence dependence of irradiation hardening in polycrystals. However, experimentally, k_y has been observed to either increase or decrease [22] suggesting that the grain size effect is not as well-established as suggested in Fig. 12.12.

12.2.5 Saturation of Irradiation Hardening

According to the dispersed barrier hardening model, Eq. (12.80), the increment in yield strength, $\Delta\sigma_y$ increases as $N^{1/2}$. In the absence of mechanisms for the destruction of obstacles, N is proportional to the total fluence and hence irradiation hardening should be proportional to $(\phi t)^{1/2}$:

$$\Delta\sigma_S \propto (\phi t)^{1/2}. \tag{12.108}$$

That is, the number of obstacles continues to increase with fluence without bound. This is clearly counter to observations of the dislocation microstructure evolution at

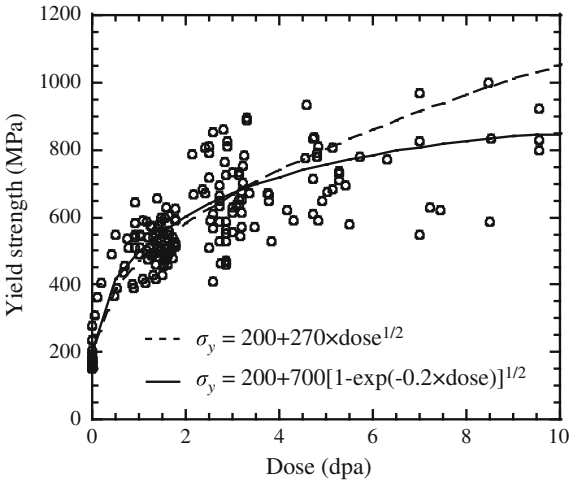

Fig. 12.14 Effect of irradiation dose on measured tensile yield strength for several 300 series stainless steels irradiated and tested at a temperature of about 300 °C (after [19])

LWR temperatures, Chap. 7, in which the dislocation loop density and size are observed to saturate by several dpa. However, at low doses, the hardening described by Eq. (12.108) is reasonably accurate. Figure 12.14 shows the irradiation hardening in 300 series stainless steels irradiated at about 300 °C and tested at about that same temperature. Note that the hardening can be fit with a $(\phi t)^{1/2}$ dependence quite well through about 5 dpa. However, the model described by Eq. (12.108) will clearly overestimate the hardening once saturation of the dislocation microstructure occurs.

In trying to account for saturation of hardening at higher doses, Makin and Minter [23] postulated that if a displacement cascade occurs in the neighborhood of an existing zone or cluster, no new zone is formed. This "prohibited" zone has a volume V. According to this model, as the concentration increases, it becomes harder to form new zones because of the reduced volume available for new zone formation. The time rate of change of the density of zones, N, is then given by:

$$\frac{dN}{dt} = \zeta \Sigma_s \phi (1 - VN), \tag{12.109}$$

where ζ is the number of zones created per neutron collision (~ 1), Σ_s is the macroscopic scattering cross section, and ϕ is the fast neutron flux. The term in parenthesis represents the fraction of solid volume available for the creation of new zones. Integration of Eq. (12.109) gives the following:

$$N = \frac{1}{V}[1 - \exp(-\zeta V \Sigma_s \phi t)], \tag{12.110}$$

and substitution of Eq. (12.110) into Eq. (12.80) yields

$$\Delta\sigma_y = A[1 - \exp(-B\phi t)]^{1/2}. \tag{12.111}$$

where $A = \alpha M \mu b \left(\frac{d}{V}\right)^{1/2}$, and $B = \zeta V \Sigma_s$. Higgy and Hammad [24] found that for 304 SS, 316 SS, and 347 SS above fluences of about 5×10^{19} n/cm^2, the irradiation hardening increment can be described by Eq. (12.111) with $B = 2$–3×10^{-21} cm^2/n. Odette and Lucas [25] found that this same equation fit the data for hardening in 300 series stainless steels irradiated and tested at about 300 °C, with $A \approx 670$ MPa and $B \approx 0.5$ dpa^{-1} with ϕt in units of dpa or $B \approx 7 \times 10^{-22}$ cm^2/n with ϕt in units of n/cm^2 and assuming that 1 dpa $\approx 7 \times 10^{20}$ n/cm^2. Note that application of Eq. (12.111) with similar values of A and B produces a good fit to the data in Fig. 12.14. Bement [26] found that for Zircaloy-2, $B = 2.99 \times 10^{-21}$ cm^2/n at 280 °C.

Fluence exponents of less than 0.5 are commonly observed. Eason [27] found in analyzing a sizable database consisting of several stainless steels that the yield strength increment at 288 °C followed a fluence dependence of the form:

$$\Delta\sigma_y = a\left(\phi t / 10^{20}\right)^b, \tag{12.112}$$

where

- for type 304 and 304L stainless steel, $a \sim 2.05$ and $b = 0.124$,
- for type 316 stainless steel $a = 0.595$ and $b = 0.491$,
- for type 316L stainless steel $a = 0.517$ and $b = 0.562$, and
- for type 347 stainless steel $a = 1.627$ and $b = 0.124$.

Williams and Hunter [21] used a modified form of Eq. (12.111):

$$\Delta\sigma_y = A[1 - \exp(-B\phi t)], \tag{12.113}$$

to fit hardening in an A533-B steel plate using $A = 22$ ksi (152 MPa) and $B = 2 \times 10^{-19}$ cm^2/n (Fig. 12.15).

Saturation occurs when a balance is reached between the creation and the destruction of obstacles. Interstitial and vacancy loops are created from defect clusters. Interstitial loops grow in size as their numbers increase. However, vacancy loops are generally unstable and shrink due to vacancy emission. Interstitial loops are removed by unfaulting. So an alternative formulation for the number of obstacles is to associate a lifetime, τ to these defects, [29] in which case, their density should develop according to:

$$\frac{dN}{dt} = \zeta \Sigma_s \phi - \frac{N}{\tau}, \tag{12.114}$$

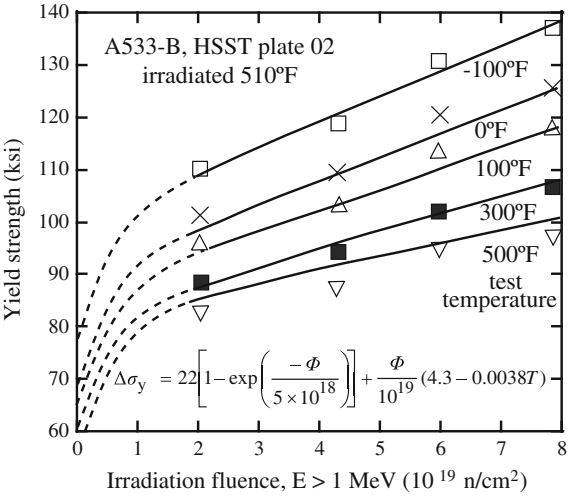

Fig. 12.15 Effect of irradiation fluence on the yield strength of A533-B steel for different test temperatures. Curves are the fits to the yield strength increment given by Eq. (12.113) (after [28])

with a solution of the form:

$$N = \zeta \Sigma_s \phi \tau [1 - \exp(-t/\tau)]. \tag{12.115}$$

12.2.6 Comparison of Measured and Predicted Hardening

The dispersed barrier hardening model has been applied to irradiation hardening of alloys in several systems. The most successful application is in the case of austenitic stainless steels and for irradiated microstructures that are dominated by loops. Figure 12.16 shows the correlation between measured and calculated yield strength for a set of solid solution alloys, which were all derived from a base alloy of composition Fe–18Cr–12Ni–1Mn, and differ in the single element added to the alloy. The alloys were irradiated with 3.2 MeV protons at 360 °C to a dose of 5.5 dpa and the microstructure was characterized by TEM. Loop and void size and density were determined for each alloy. Only the base 316 stainless steel alloy, 316 + Mo, and 316 + Ni/Cr contained voids. The measurements of yield strength in Fig. 12.16 actually come from microhardness indentations (discussed in Sect. 12.2.8) and the calculated hardness values are determined from the dispersed barrier hardening model, Eq. (12.80). In this case, $\alpha = 0.25$ for loops and $\alpha = 0.5$ for voids produced the best fit with the data.

The loop strength of 0.25 is consistent with, although on the low side, of what has been observed in the literature [3, 13, 17, 31–34]. Values of α for loops as high as 0.5 have been deduced from strengthening data [35]. The value of α for voids (0.5) is half that of the theoretical value for Orowan strengthening. However, Ando et al. [36] have shown that cavity shearing is more likely than Orowan pinning,

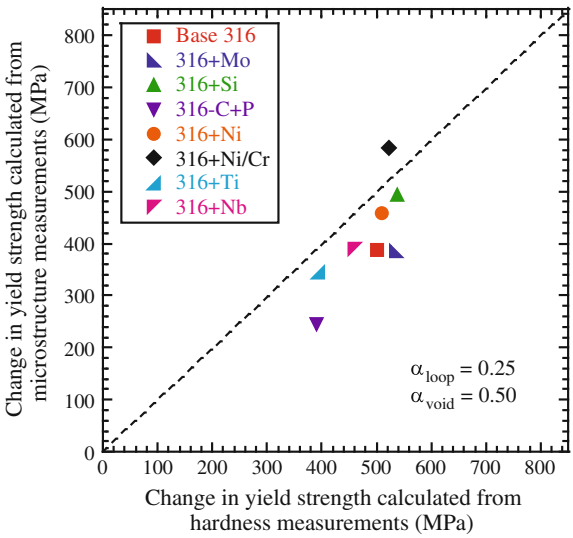

Fig. 12.16 Correlation between measured and calculated yield strength using Eq. (12.80) (after [30])

resulting in a value of $\alpha = 0.5$ rather than 1.0. They concluded that the high value of α observed in some experiments is likely due to cavity–precipitate association. Electron microscopy has revealed that bubbles and MC precipitates nucleate and grow together in austenitic stainless steels [37]. Kelly [38] considered the hardening to be due to two spheres in contact rather than a single obstacle and derived the following relation for the bubble–precipitate pair:

$$\Delta\sigma_{\text{bubble-ppt}} = \frac{0.16M\mu b\sqrt{Nd}}{1 - \frac{\sqrt{6}}{3}\sqrt{Nd}} \ln\left(\frac{\sqrt{6d}}{3b}\right). \tag{12.116}$$

Hardening in ferritic steels used in reactor pressure vessels can be very complicated due to the role of solutes such as copper, nickel, and manganese, and the roles of temperature and irradiation flux. Hardening in RPV steels is controlled by the evolution of two primary classes of ultra-fine scale features: copper-rich precipitates (CRP) and matrix features (MF) [39]. The latter class can be subdivided into unstable matrix features (UMF) and stable matrix features (SMF), such that MF = UMF + SMF. CRPs form from a supersaturated solid solution as a consequence of radiation-enhanced diffusion. These precipitates are extremely small and are best described as nanoscale defects and contribute the largest amount to hardening (Fig. 12.17). They are the dominant feature in irradiated RPV steels that have Cu contents greater than about 1 %. Their size and volume fraction increase with Cu content above about 1 %, but the number density is relatively insensitive to copper in the range 0.2–0.4 %. As such, their significance in hardening increases up to about 0.25–0.35 % Cu [16]. CRPs can also become enhanced in Ni and Mn depending on the amount of these solutes in the steel.

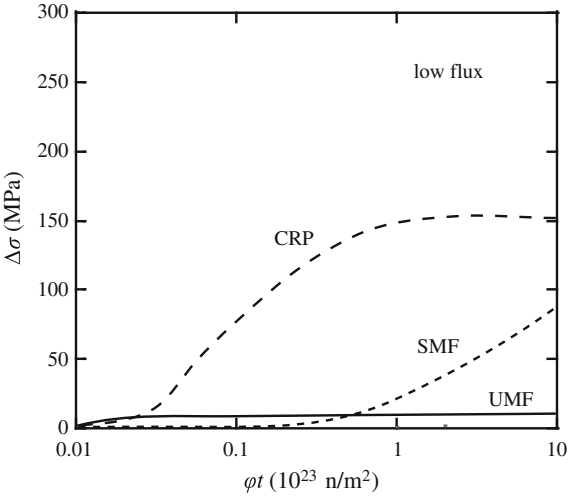

Fig. 12.17 Components of the microstructure contributing to hardening of a ferritic pressure vessel steel (after [40])

SMFs are not completely understood, but likely consist of a range of defect cluster–solute complexes whose exact natures depend on the metallurgical variables and irradiation conditions. Phosphides, carbonitrides, manganese-rich phases, large vacancy clusters, and immobile interstitial loops are all likely candidates for the SMFs. SMFs account for the residual hardening in low Cu steels. UMFs undergo recovery during irradiation and likely consist of small vacancy and interstitial clusters produced directly in displacement cascades.

The increase in yield strength in RPV steels due to irradiation can be described by the following [41]:

$$\Delta\sigma_{\mathrm{y}} = \Delta\sigma_{\mathrm{yp}} + B\sqrt{\phi t}, \tag{12.117}$$

where $\Delta\sigma_{\mathrm{yp}}$ is the contribution from CRPs and $B\sqrt{\phi t}$ is due to SMFs. The parameter B in the second term contains the composition dependence of hardening due to SMFs and will vary between steels. Odette et al. [41] have identified the composition dependence of B for low Cu steels (<0.1 %) to be:

$$B = 681\mathrm{P} + 460\mathrm{Cu} + 10.4\mathrm{Ni} + 10.7\mathrm{Mn} - 10\,[\mathrm{MPa}]. \tag{12.118}$$

Figure 12.18 shows the very strong dependence of hardening on copper content, which has a profound impact on RPV steels and welds.

Dose rate affects the yield strength increment through the term $\Delta\sigma_{\mathrm{yp}}$. Odette [41] has shown that higher dose rates shift the yield strength to higher fluences (Fig. 12.19(a)) in the preplateau region. The CRP term can be written as follows:

$$\Delta\sigma_{\mathrm{yp}}(\phi t_{\mathrm{e}}) = \Delta\sigma_{\mathrm{ypm}}\sqrt{X}, \tag{12.119}$$

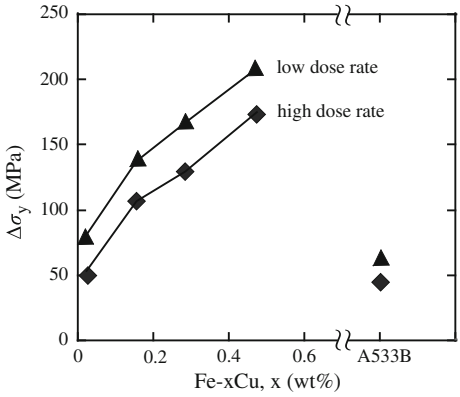

Fig. 12.18 Effect of copper on the hardening of ferritic steel alloys (after [42])

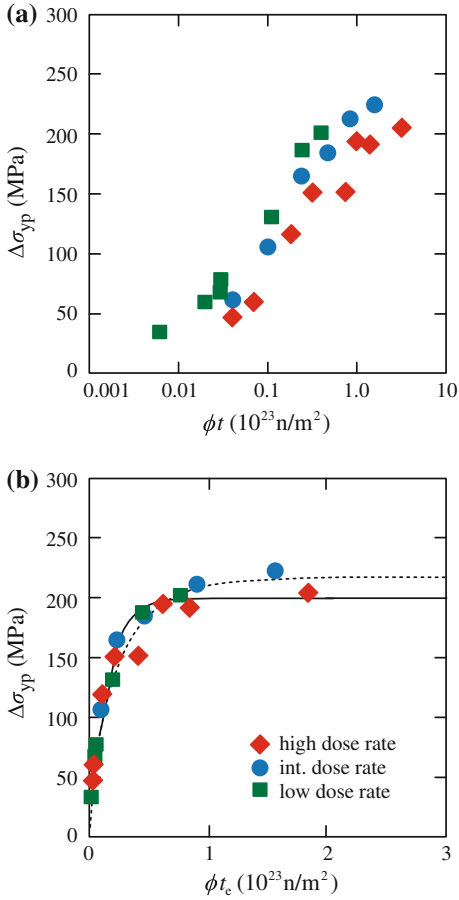

Fig. 12.19 Hardening of an A533B-type bainitic steel containing 0.4 % Cu and 1.25 % Ni following irradiation at 290 °C (**a**) due to copper-rich precipitates versus fluence, and (**b**) due to copper-rich precipitates versus *effective* fluence (after [41])

where $\Delta\sigma_{ypm}$ is the plateau value of hardening (relatively insensitive to dose rate), ϕt_e is an effective fluence defined by $\phi t_e \approx \phi t(\phi_r/\phi)^{1/2}$, and ϕ_r is a reference flux.

The term X is given by:

$$X = \left\{1 - \exp\left[-(F\phi t_e)^{\beta}\right]\right\}, \tag{12.120}$$

where F and β are the fitting parameters. The result is that the CRP contribution to yield strength can be expressed as a function of ϕt_e (Fig. 12.19(b)) which shows that the CRP increment can be accounted for by using the effective fluence.

Attempts to apply the dispersed barrier hardening model to predict hardening in irradiated ferritic-martensitic steels have met with less success as the result is generally less than the measured value by a significant amount [43, 44].

12.2.7 Radiation Anneal Hardening

An additional hardening mechanism occurs upon annealing of bcc metals following irradiation and is known as radiation anneal hardening (RAH) [45]. Figure 12.20 shows the yield strength as a function of annealing temperature following irradiation of niobium containing 35 wppm C and 41 wppm O to a fluence of 2×10^{18} n/cm^2. Note that hardening begins at a temperature of about 120 °C and increases to a maximum at about 180 °C before decreasing. However, a second peak in hardening appears at a temperature of 300 °C before the yield strength drops due to recovery. These peaks in the hardness are attributed to the oxygen and carbon impurities in the metal. It is well known that interstitial impurities increase the yield strength of bcc metals. In the irradiated state, the radiation-produced defects serve as trapping centers for interstitial impurities. Annealing enables the migration of the interstitials to defect clusters resulting in the formation of

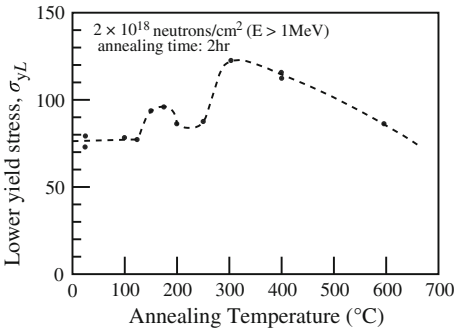

Fig. 12.20 Radiation anneal hardening in niobium containing 35 wppm C, 41 wppm O, and 5 wppm N following irradiation to 2×10^{18} n/cm^2 and annealing for 2 h. Unirradiated yield strength is ~40 MPa (after [46])

impurity–defect complexes or the strengthening of existing defect clusters, both of which act as barriers to slip dislocation motion.

In the example shown in Fig. 12.20, the first peak is due to the migration of oxygen to defect clusters and the second peak is due to the migration of carbon. Measurements of the change in resistivity with time at temperature can be used to determine the activation energy for resistivity change, which can then be compared with the activation energy for diffusion of the impurities to determine their identity. In niobium, vanadium, and iron alloys, the primary agents responsible for RAH are oxygen, carbon, and nitrogen.

12.2.8 The Correlation Between Hardness and Yield Strength

Much data on hardening come from indentation or shear punch measurements of irradiated samples. Indentation techniques include Vickers microhardness and ball indentation. The Vickers microhardness technique uses a diamond pyramid-shaped indenter tip that is pressed against the sample with a predetermined load (Fig. 12.21(a)). The shape of the indent and the magnitude of the load determine the

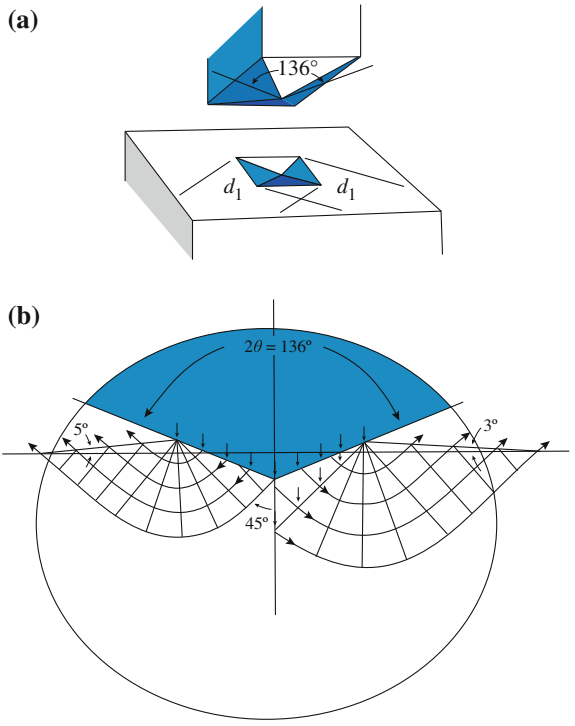

Fig. 12.21 Illustration of (**a**) the diamond pyramid tip used in Vickers microhardness measurement and the tip impression in the sample, and (**b**) flow pattern during Vickers indentation of a metal (after [47])

value of hardness, which is a measure of the resistance of the solid to deformation. The shear punch test is essentially a blanking operation in which a flat punch is driven at a constant rate through a TEM-sized disk. The disk is constrained along both its upper and lower surfaces in a test fixture, which also guides the punch. The load on the punch is measured as a function of specimen displacement, which is taken to be equivalent to the crosshead displacement. The yield and maximum loads are taken from a plot of punch load versus punch displacement. All of these techniques enjoy advantages over tensile testing in that they are relatively simple and quick, require much smaller volumes of irradiated materials, and in the case of microhardness indentation, are compatible with ion irradiation in which the damage is confined to the surface region. However, as hardening is generally defined as the increment in the yield strength due to the irradiated microstructure, there is much interest in relating hardness measurements to yield strength in order to increase its utility.

As originally described by Tabor [48], the indentations made during hardness tests are discernible as permanent impressions in the metal, so that the indentation is primarily a measure of the plastic properties of the metal. While it is true that some changes in shape and size occur when the indenter is removed, the overriding effect is the plastic flow of the metal around the indenter tip, implying that the mean pressure over the indenter is connected to the plastic rather than elastic properties of the metal. Tabor [48] showed that this is indeed the case for a variety of different hardness and scratch tests, based on the work of Prandtl [49] and Hencky [50] and that the hardness measurement can also be used as a measure of the yield stress of the metal.

During indentation, stress is applied to the metal surface through the indenter tip. However, since the tip surface is not parallel to the sample surface, the stress state during indentation is not simply compressive. Instead, the stresses must be examined in two dimensions (along and perpendicular to the axis of the indenter tip). Plastic deformation during indentation occurs when the Huber–Mises criterion is satisfied, which in the two-dimensional case occurs when the maximum shear stress reaches a critical value, k:

$$2k = 1.15\sigma_{\mathrm{y}}, \tag{12.121}$$

where σ_{y} is the yield stress.

The pyramidal shape of the indenter tip can be treated as a wedge during indentation. The pattern of plastic flow around the indenter tip during indentation can be determined using the Prandtl solution [49]. The flow pattern is shown schematically in Fig. 12.21(b) for a Vickers indentation. The pressure normal to the surface of the indenter tip P can be calculated as:

$$P = 2k(1 + \pi/2). \tag{12.122}$$

Equations (12.121) and (12.122) can be combined to yield:

$$P = 2k(1 + \pi/2) = 1.15\sigma_y(1 + \pi/2) = 2.96\sigma_y. \tag{12.123}$$

For a Vickers indenter:

$$H_v \equiv \frac{\text{load}}{\text{contact area}} = 0.927P, \tag{12.124}$$

where 0.927 is the ratio of the area of the base of the pyramid (the projected area) to the area of the sides of the pyramid (contact area). Combining Eqs. (12.123) and (12.124) gives the following:

$$H_v = 0.927P = 0.927 \times 2.96\sigma_y = 2.74\sigma_y. \tag{12.125}$$

Writing this expression in terms of yield strength gives the correlation:

$$\sigma_y = CH_v, \quad \text{with} \tag{12.126}$$

$C = 0.364$ for σ_y and H_v in units of kg/mm^2, and
$C = 3.55$ for σ_y in MPa and H_v in kg/mm^2

Tabor found the same result experimentally for a variety of metals (aluminum, copper, and mild steel). More recently, Larsson [51] studied indentation tests both theoretically and numerically. Specifically, he used finite element analysis to examine elastic–plastic material behavior under sharp contact situations (nanoindenters, Vickers or cone indenters, or even gear contact). Larsson's finite element results were in good agreement with the results of Tabor, validating the assertion that yield stress can, indeed, be determined from Vickers hardness measurements.

Busby et al. [52] reviewed existing correlations and compiled hardness data on austenitic stainless steels and ferritic steels to empirically determine the correlation between hardness and yield strength. In general, austenitic stainless steels follow a relation of the form:

$$\Delta\sigma_y = 3.03\Delta H_v, \tag{12.127}$$

and ferritic steels obey a correlation of the form:

$$\Delta\sigma_y = 3.06\Delta H_v. \tag{12.128}$$

Figure 12.22(a, b) shows these correlations for the two classes of steels. The correlations are extremely close and can be taken to be equivalent given the confidence interval used. While the dataset is best fit with a linear relation, the authors noted

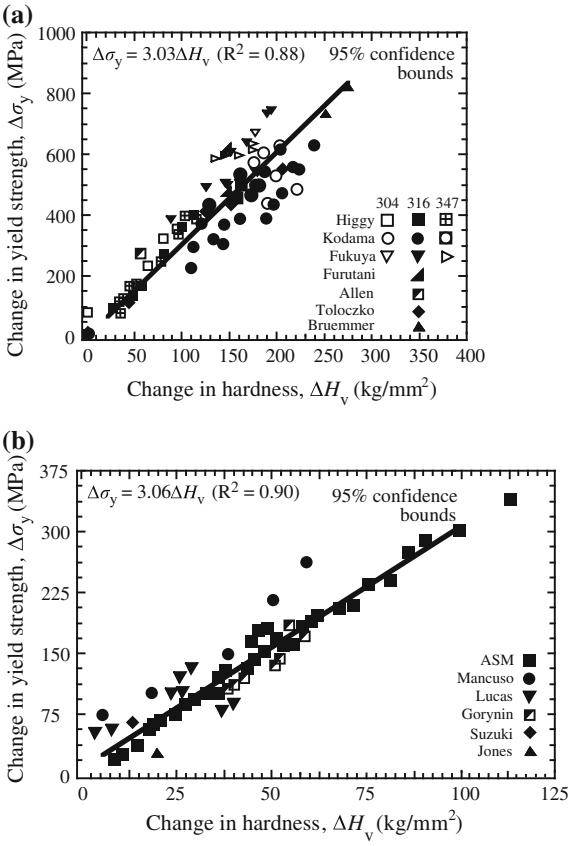

Fig. 12.22 Experimental data plotted as a change in yield stress versus change in hardness for (**a**) austenitic stainless steels and (**b**) ferritic steels. The hardness-yield stress correlation is also plotted along with 95 % confidence bounds (after [52])

that for austenitic stainless steels, there is some indication of a reduction in slope with increasing values of hardness. A two-slope fit resulted in:

$$\begin{aligned} \Delta\sigma_y &= 3.63\Delta H_v \qquad \Delta H_v < 100 \text{ kg/mm}^2 \\ \Delta\sigma_y &= 2.13\Delta H_v + 155 \quad \Delta H_v > 100 \text{ kg/mm}^2. \end{aligned} \tag{12.129}$$

The slope of the correlation in the low-load regime is close to Tabor's theoretical value of 3.55 with the difference attributed to scatter in the database. The lower value of the slope at higher loads may reflect the differences between a hardness test and a tensile test. While the yield stress is measured at approximately 0.2 % strain, the hardness test involves much higher strains, estimated to be between 8 and 18 % [48, 51]. Thus, the nature of deformation of the irradiated metal will influence the correlation between hardness and yield strength at the higher hardness levels.

A correlation coefficient of 3.5 has been shown to fit a wide range of RPV steel data [53]. It should also be noted that this data is best fit with a simple linear regression that intersects the ordinate at about 30 MPa at a ΔH_v of zero, which

could be a consequence of the fact that ΔH_v values correspond to a flow stress of several percent plastic strain. At low levels of hardening, σ_y may increase due to dislocation cutting of small defects, without a measurable increase in ΔH_v. At the higher levels of hardening reached when defects are harder, the flow stress rises in proportion to the yield stress.

12.3 Deformation in Irradiated Metals

In addition to undergoing hardening, irradiated metals experience a loss of ductility and a loss of work hardening. The loss of ductility with dose in austenitic steels irradiated and tested at ~300 °C is shown in Fig. 12.23. Note that ductility drops from some 20–30 % to values of less than 1 % by ~4 dpa. The decrease in work hardening is evident by the decrease in the difference between σ_{UTS} and σ_y with increasing irradiation dose as shown in Fig. 12.1(a–d). If the stress–strain behavior of the metal follows the power law hardening model given in Eq. (12.27), $\sigma = K\varepsilon^n$, then, as shown in Eq. (12.57), the true uniform elongation ε_u is equal to n. So to first order, variations in ε_u with irradiation follow the changes that occur to the work hardening behavior described by n. The behavior of ε_u versus dose for stainless steel over the temperature range 300–500 °C can be described by the curves in Fig. 12.24(a). The uniform elongation decreases significantly and approaches a minimum at a dose that decreases with temperature down to 300 °C. The temperature dependence of the loss of ductility is shown more clearly in Fig. 12.24(b). As core components in light water reactors are generally at temperatures around 300 °C, the minimum in ductility at that temperature is a major concern.

The loss of uniform ductility and work hardening are due to the same cause: the interaction between dislocations and the irradiated microstructure. Up to this point, we have only discussed how irradiation can lead to hardening by pinning of

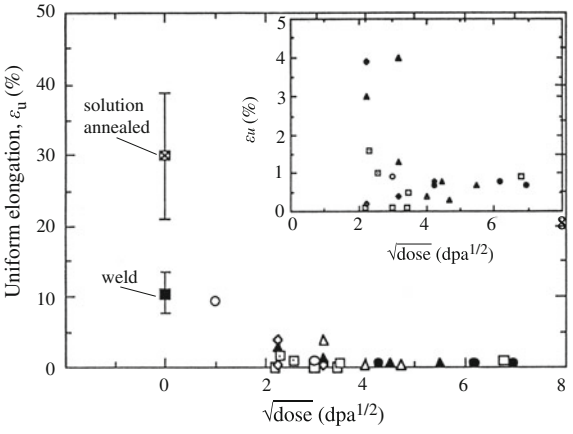

Fig. 12.23 Uniform elongation as a function of the square root of dose for 300 series austenitic stainless steels irradiated and tested at ~300 °C (after [25])

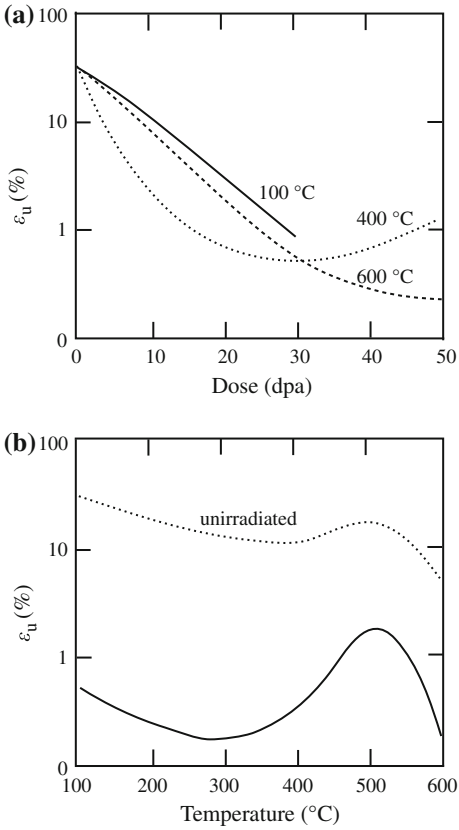

Fig. 12.24 Variation of uniform ductility in austenitic stainless steel with (**a**) dose and temperature, and (**b**) temperature (after [17])

dislocations by obstacles. However, dislocation–loop interaction can result in unfaulting of the loop and incorporation into the dislocation network. In fcc metals, unfaulting of a Frank loop can occur by several mechanisms. In one such mechanism [54], a mobile dislocation with Burgers vector $a/2[\bar{1}01]$ (shown as *DB* in Fig. 12.25(a)) intersects a small Frank loop with Burgers vector $a/3[\bar{1}11]$ ($D\delta$ in Fig. 12.25(a)) to form a Shockley partial on the loop plane with Burgers vector $a/6[\bar{1}\bar{2}1]$ (δB in Fig. 12.25(a)). The interaction of the Shockley partial with the faulted loop generates a helical segment on the original dislocation with Burgers vector $DB = D\delta + \delta B$, and eliminates the loop.

A second type of reaction occurs when a glissile, perfect dislocation, $a/2[\bar{1}\bar{1}2]$ interacts with a sessile $a/3[111]$ Frank loop creating an $a/6[\bar{1}\bar{1}2]$ dislocation according to $a/2[\bar{1}\bar{1}0] + a/3[111] = a/6[\bar{1}\bar{1}2]$[55]. The Shockley partial created by the interaction can sweep across the Frank loop, removing the stacking fault and reacting with the opposite side of the Frank loop according to $a/6[\bar{1}\bar{1}2] + a/3[\bar{1}\bar{1}\bar{1}] = a/2[\bar{1}\bar{1}0]$. Figure 12.25(b) shows the process by which the Frank loop lying in the plane of the figure interacts with a perfect dislocation moving on some other plane. The Frank loop is annihilated and the only remnant is a coil in the $a/2[\bar{1}\bar{1}0]$

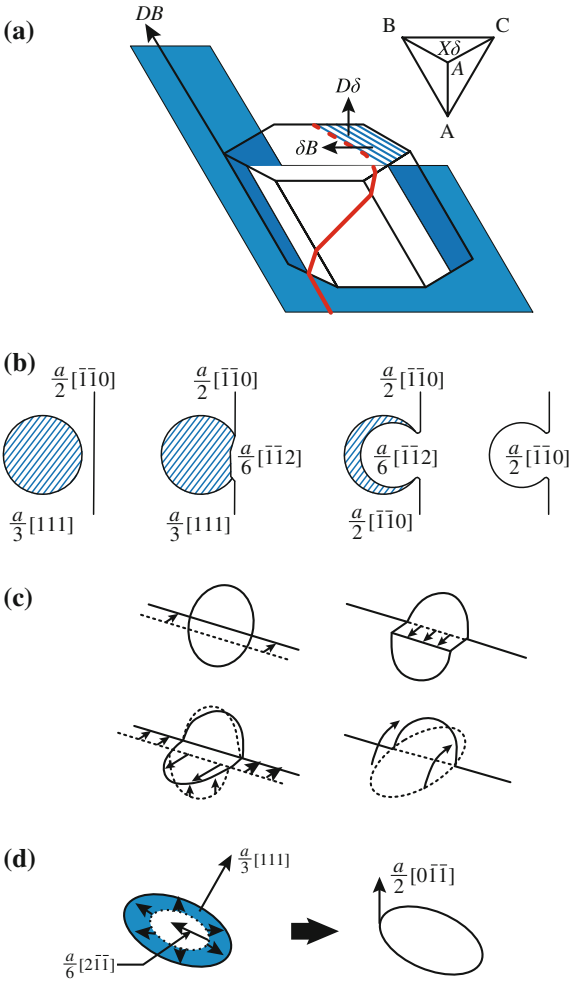

Fig. 12.25 Loop unfaulting mechanisms proposed by (**a**) Strudel and Washburn [54]. (**b**) Gelles [55]. (**c**) Foreman and Sharp [56], and (**d**) Tanigawa [57]

dislocation approximately on the Frank loop {111} plane. The result is that the unfaulting product of a perfect dislocation–Frank loop interaction immediately becomes part of the perfect dislocation network.

A third mechanism [56] involves intersection of a mobile dislocation with a loop in which the loop glides on itself and becomes part of the glide dislocation as shown in Fig. 12.25(c). Finally, unfaulting can be triggered by the formation of a Shockley partial loop inside a Frank loop [57]. Reaction between the Shockley partial loop of the type $a/6[11\bar{2}]$ and the Frank loop proceeds according to: $a/6[11\bar{2}] + a/3[111] = a/2[110]$ and is shown in Fig. 12.25(d).

In bcc metals, faulted loops are rarely observed because of the high stacking-fault energy that causes unfaulting at very small loop sizes. The Frank loop is of the form $a/2[110]$, and the stacking fault can be removed by two possible

unfaulting reactions [58]: $a/2[110] + a/2[00\bar{1}] \rightarrow a/2[11\bar{1}]$, or $a/2[110] + a/2[\bar{1}10] \rightarrow a/2[010]$, with the result being a perfect loop in either case. The result of each of these unfaulting reactions is the removal of the dislocation loop from the microstructure and the growth of the dislocation network density.

12.3.1 Localized Deformation

Multiple shearing can eliminate defect clusters and coherent precipitates in the dislocation glide plane. So in fact, passage of an initial group of dislocations down a particular slip plane can result in the clearing of the obstacles in that slip plane so that subsequent dislocations can pass relatively unimpeded. First observed in the 1960s in bcc metals [59, 60], this process is referred to as *dislocation channeling*, which occurs in fcc, bcc, and hcp crystal lattices. As a result of channeling, work hardening in channels drops to nearly zero along with the macroscopic uniform strain, as the deformation becomes highly localized within the channels. Byun et al. [61] have pointed out that channel deformation occurs in unirradiated metals at high stress, and that the common feature between channel deformation in irradiated and unirradiated metals is the high stress.

Dislocation channels are characterized by width, spacing, and the amount of strain in the channel. Figure 12.26 shows TEM images of dislocation channels in Fe–18Cr–12Ni irradiated to 5.5 dpa at 360 °C with 3 MeV protons and strained to 7 % at 288 °C. Note in Fig. 12.26(b) the contrast difference between the channel and the matrix, indicating that the channel has been cleared of most of the obstacles. Channel width is generally on the order of 0.1 μm and channels are typically spaced 1–3 μm apart. Channels propagate across grains, initiating and terminating at grain boundaries. In a tensile sample, the channels of surface grains produce a step on the surface. Figure 12.27 shows an SEM image of the surface of irradiated stainless

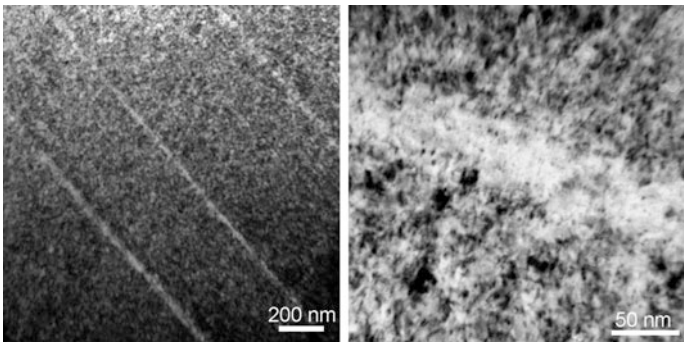

Fig. 12.26 Transmission electron micrographs of dislocation channels in Fe–18Cr–12Ni irradiated to 5.5 dpa at 360 °C with 3 MeV protons and strained to 7 % at 288 °C (courtesy of Z Jiao, University of Michigan)

Fig. 12.27 Scanning electron micrograph of dislocation channels intersecting the surface of austenitic stainless steels irradiated to 5.5 dpa with 3.2 MeV protons at 360 °C followed by straining at 3×10^{-7} s^{-1} to 7 % plastic strain in 288 °C argon (courtesy of Z Jiao, University of Michigan)

steel samples strained to 7 %, from which the magnitude of the surface step can be characterized using Atomic-force microscopy (AFM). Figure 12.28 shows how the intersection of a channel with the surface produces a step of height, h due to the passage of dislocations down the channel. For a step height, h, and a width, w, the channel strain, γ, is simply:

$$\gamma = h/w. \tag{12.130}$$

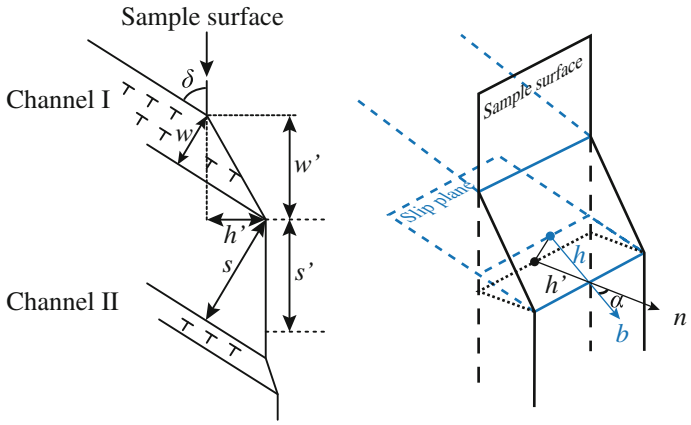

Fig. 12.28 Intersection of dislocation channels with a surface creating a step on the surface. Primed quantities are *apparent* values of height, h', width, w', and spacing, s', that are measured directly and must be converted to true height, h, true width, w, and spacing, s, to determine the strain in the channel (after [62])

However, measurement of the channels on the surface will provide apparent values of height, h', width, w', and spacing, s', that must be converted to true values using [62]:

$$\begin{aligned} w &= w' \sin(\delta) - h' \cos(\delta) \\ h &= h' / \cos(\alpha), \end{aligned} \tag{12.131}$$

where δ is the angle between dislocation slip plane and the sample surface and α is the angle between the dislocation slip direction and the surface normal.

The number of dislocations in a channel, n, can be related to the step height by $n = h/b$, where b is the Burgers vector. Was et al. [62] have shown that straining 316L stainless steel to about 7 % applied strain following irradiation to 5.5 dpa at 360 °C resulted in an average channel strain of close to 100 % caused by the passage of over 1000 dislocations down the channels. The great majority (>90 %) of total strain in the solid occurs in the channels, meaning that irradiated materials act like a multilayered solid (such as a metal-ceramic multilayered material) in which all strain occurs in the softer layer. Observations and model calculations indicate that many fewer dislocations (a few to 50) remain in the channels [62, 63]. Two possible reasons for the low number of residual dislocations in the channels are slip transfer to neighboring grains in cases where the slip planes are closely aligned between grains, or reaction of the dislocation with the grain boundary. When a dislocation channel intersects a grain boundary, dislocations in the channel either transfer to an adjoining grain or pile up at the grain boundary. When a dislocation transfers, it leaves a residual dislocation in the grain boundary. The reaction of dislocations involving grain boundaries can be expressed as: $\boldsymbol{b}_r = \boldsymbol{b}_1 - \boldsymbol{b}_2$, where $\boldsymbol{b}_r$ is the Burgers vector of the residual dislocation left behind in the grain boundary, and $\boldsymbol{b}_1$ and $\boldsymbol{b}_2$ are the Burgers vectors of dislocations in grains 1 and 2, respectively. The number of residual dislocations in a grain boundary is likely proportional to the channel height or channel strain as the portion of dislocations piled up at a grain boundary is relatively small.

An example of dislocation interaction with precipitates is shown in Fig. 12.29. This is an APT image of a dislocation channel in a field of radiation-induced

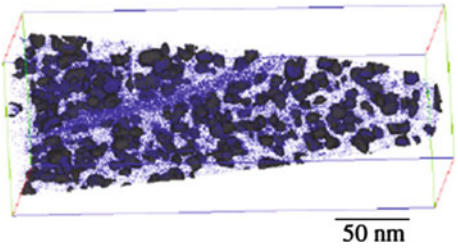

Fig. 12.29 Atom map of Si in a dislocation channel in a 304 SS alloy containing 1 % Si after irradiation to 5 dpa at 360 °C and straining to 6 % at 288 °C (after [64])

Ni-/Si-rich precipitates in a high-purity 304 stainless steel alloy containing ~1 at.% Si irradiated to 5 dpa at 360 °C with 2 MeV protons, and followed by straining to 6 % at 288 °C [64]. The image shows an atom map of Si. Precipitates are identified by regions with Si concentration ≥5 at.% and appear as dark clusters, while Si atoms appear as small purple dots. Quantitative chemical analysis, represented by the density of dots, indicate that the concentration of Si in the channel is greater than that in the bulk and much greater than that between precipitates. These observations indicate that the passage of dislocations induced dissolution of the precipitates in the channel, providing a path of lower resistance for subsequent dislocations.

A second example shows that dislocation cutting of voids does not result in their removal [65]. Figure 12.30 shows two images of a dislocation channel in a high-purity Fe–18Cr–12Ni alloy irradiated with 2 MeV protons to 5 dpa at 360 °C and strained to 7 % at 288 °C. Note in the left-hand image that the dislocation channel appears to be relatively free of dislocation loops, discernable from the reduction in contrast in the channel verses that outside the channel. The same region imaged in a slightly underfocused condition shows that voids are still present in the channel, and at a density that is similar to that outside the channel. These observations indicate that voids can survive in channels when deformation occurs at temperature.

In addition to channeling caused by gliding dislocations, deformation twinning is also observed to occur. Deformation twinning or mechanical twinning is a localized deformation mechanism caused by partial dislocations. In fcc metals with low stacking-fault energy (SFE), deformation twins are formed by the glide of Shockley partial dislocations of the same sign on successive {111} planes. In these twins, the shear strain is 70.7 % and the defects are cleared by glide of the partial

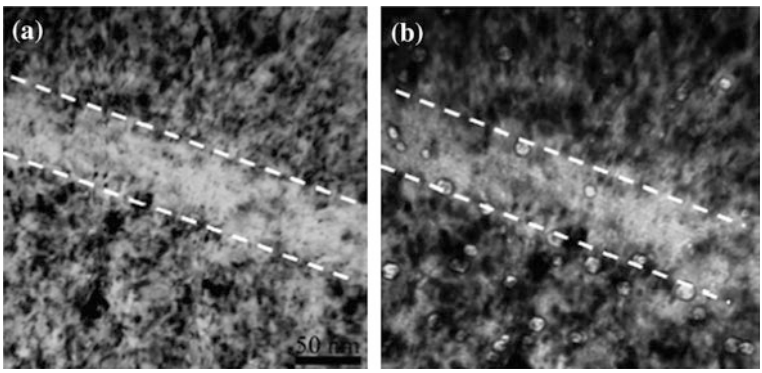

Fig. 12.30 TEM image of a dislocation channel in an Fe–18Cr–12Ni alloy irradiated to 5 dpa at 360 °C and strained to 7 % at 288 °C showing (**a**) the cleared channel, and (**b**) voids in the channel visible in the underfocused condition (after [65])

dislocations [66]. The Shockley partials are formed from dissociation of the ordinary dislocation with Burgers vector 1/2 ⟨110⟩ into leading and trailing partial dislocations with Burgers vector of the type 1/6 ⟨112⟩. The separation of the partials or the width of the stacking fault, d, is given by:

$$d \approx \frac{\mu b^2}{4\pi\gamma_{\mathrm{SFE}}}, \tag{12.132}$$

where γ_{SFE} is the stacking-fault energy. In low stacking-fault energy metals, the separation of partials is large. Was et al. [62] have observed the formation of twins at the intersection of dislocation channels with grain boundaries where the stress and strain is the greatest. Whether by channeling or twinning, localized deformation increases strongly with dose. Twinning is also favored at low temperatures.

12.3.2 Deformation Mechanism Maps

As described in Chap. 7, plastic deformation is characterized by the shear stress, strain or strain rate, and temperature. Frost and Ashby [67] classified deformation mechanisms into five groups:

1. Flow above the ideal shear strength
2. Low-temperature plasticity by dislocation glide
3. Low-temperature plasticity by twinning
4. Power law creep by dislocation glide or climb and glide
5. Diffusional creep

Each of these mechanisms can be subdivided into additional mechanisms. When stress and temperature are the independent variables, then the response of the metal is the strain rate and strain. Alternatively, the temperature and strain rate could be selected as the independent variables and the stress constitutes the response of the metal.

If strain rate is selected as the dependent variable, a convenient method of relating the strain rate of a metal to the independent variables of shear stress and temperature is the deformation mechanism map. A deformation mechanism map is a representation of the mechanism of deformation in stress-temperature space where shear stress, σ_s, is represented by the normalized stress, σ_s/μ, where μ is the shear modulus, and temperature is represented by the homologous temperature, T/T_m, where T_m is the melting temperature. The map provides a relationship between the two independent variables σ_s and T and the dependent variable, $\dot{\varepsilon}$. An example of such a map for 316 stainless steel is given in Fig. 12.31(a), in which the normalized stress is plotted on the ordinate and the homologous temperature is plotted on the

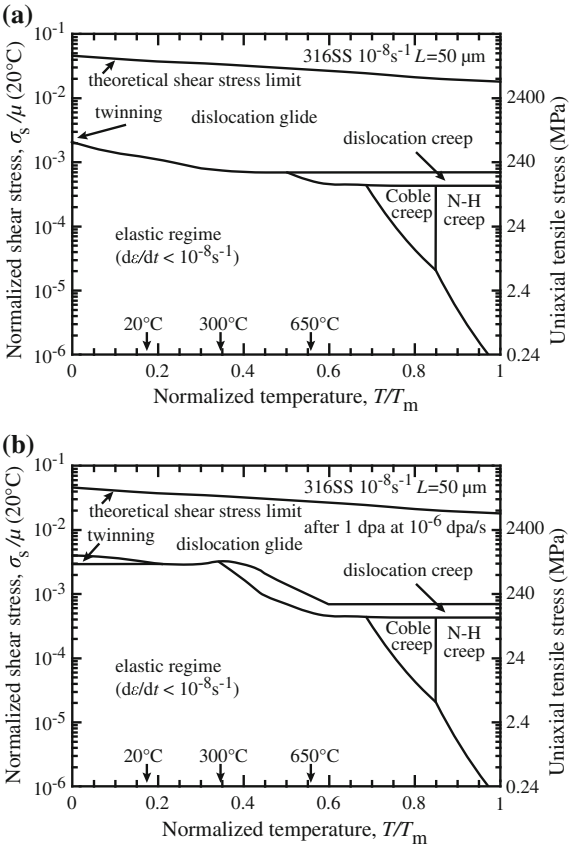

Fig. 12.31 Deformation mechanism map for 316 stainless steel with a grain size of 50 μm and deformed at a strain rate of 10^{-8} s^{-1} for (**a**) unirradiated condition, and (**b**) irradiated to 1 dpa at 10^{-6} dpa/s (after [68])

abscissa. The various deformation mechanisms are denoted by labeled regions in the map, and the strain rate response of the metal to the stress/temperature combinations is given by contours of equistrain rate. Essentially, the strain rate contours provide the constitutive law in the form of a single equation:

$$\dot{\varepsilon} = f(\sigma_s, T). \tag{12.133}$$

Figure 12.31(a) shows that above the ideal shear strength, plastic collapse occurs and the strain rate approaches infinity:

$$\begin{aligned} \dot{\varepsilon} &= \infty \quad \text{for } \sigma_s \geq \alpha\mu \\ \dot{\varepsilon} &= 0 \quad \text{for } \sigma_s < \alpha\mu, \end{aligned} \tag{12.134}$$

where α depends on the crystal structure and instability criterion but is generally between 0.05 and 0.1. Below the ideal shear strength, flow can occur by glide of dislocations that is generally limited by obstacles. Ashby gives the strain rate in the discrete obstacle controlled plasticity regime as:

$$\dot{\varepsilon} = \dot{\varepsilon}_0 \exp\left[-\frac{Q}{kT}\left(1 - \frac{\sigma_s}{\sigma_s^0}\right)\right], \tag{12.135}$$

where Q is the activation energy required to overcome the obstacle without aid from external stress, and σ_s^0 is the athermal component of the flow stress. At low-temperature and high normalized stress, twinning is observed to occur. Byun et al. [63] have characterized the deformation in terms of the stress and strain, and have determined that the twinning stress σ_t in polycrystalline metals could be defined by the critical stress for infinite separation of partials:

$$\sigma_t = 6.14\frac{\gamma_{SFE}}{b}, \tag{12.136}$$

where b is the Burgers vector of the partial dislocation. The strain rate equation for twinning [67] is given as:

$$\dot{\varepsilon} = \dot{\varepsilon}_t \exp\left[-\frac{Q_t}{kT}\left(1 - \frac{\sigma_s}{\sigma_t}\right)\right], \tag{12.137}$$

where Q_t is the activation free energy to nucleate a twin without the aid of external stress, σ_t is the stress required to nucleate twinning in the absence of thermal activation, and $\dot{\varepsilon}_t$ is a constant. The balance of the deformation map refers to creep mechanisms and these are discussed in detail in Chap. 13.

The effect of irradiation at a strain rate of 10^{-8} s^{-1} is shown in Fig. 12.31(b). Due to irradiation hardening at temperatures below about $0.5T/T_m$, the stress for dislocation glide is increased, reducing the dislocation glide regime. Above this temperature, irradiation-enhanced softening can occur, causing a reduction in the stress for dislocation glide and an expansion of the glide regime at high temperature. At low temperatures and high stresses, twinning can occur.

Byun and Hashimoto [69], and Farrell et al. [70] have constructed deformation mode maps for irradiated alloys that describe the mode of deformation as a function of applied strain. The stress-based map is shown in Fig. 12.32(a) and the strain-based map is shown in Fig. 12.32(b) for 316 austenitic stainless steel. In the stress-based map, higher dose leads to an increase in yield strength and an increase in the elastic deformation regime.

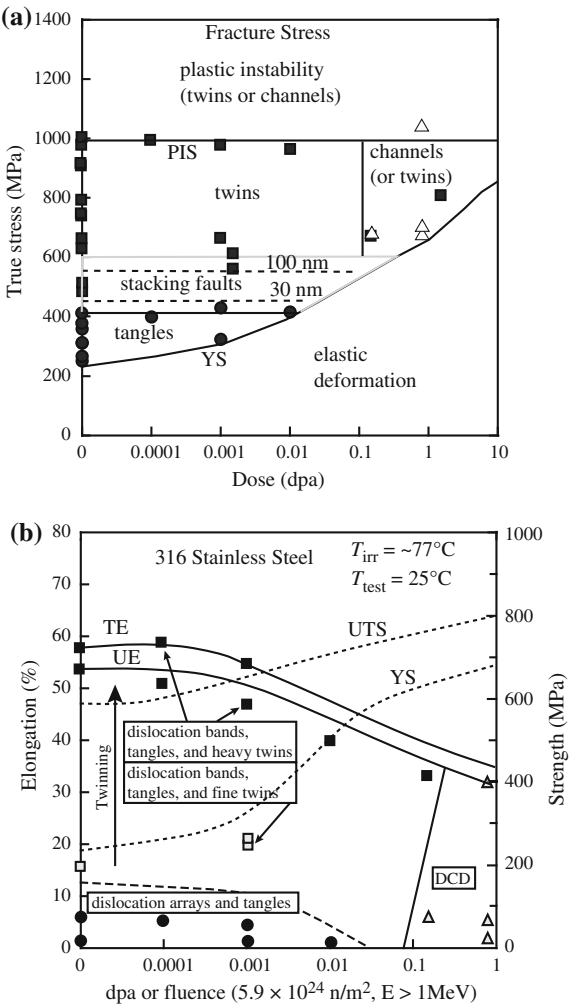

Fig. 12.32 (**a**) Stress-based deformation mode map for 316 stainless steel in true stress-dose space (PIS plastic instability stress) (after [69]). (**b**) Strain-based deformation mode map for 316 stainless steel neutron irradiated at 65–100 °C and tested at room temperature (TE total elongation, UE uniform elongation, DCD dislocation channeling deformation) (after [70])

Nomenclature

A	Area of slip plane or dislocation loop or cross-sectional area of a tensile sample after straining
A_0	Original cross-sectional area in a tensile sample
$\boldsymbol{b}$	Burgers vector
d	Grain size or obstacle diameter or separation distance of partial dislocations
e	Elastic strain
E	Elastic modulus
F	Force
h	Dislocation channel height
H_v	Vickers hardness

K Bulk modulus or constant in power law hardening equation
k Square root of second invariant of the stress deviator used for the von Mises yield criterion
k_y Unpinning stress
L_0 Original length of a tensile sample
L Deformed length of tensile sample. Also length of dislocation pileup on a slip plane
l Distance between obstacles on the slip plane
m Schmidt factor
M Taylor factor
N Number density of obstacles on a slip plane
n Number of dislocations in a pileup
p Hydrostatic pressure
P Load
r Distance from obstacle to Frank–Read source
r_d Dislocation core radius
R Radius of an obstacle
S Engineering stress, or weighting parameter from Eq. (12.103)
t Time
T Temperature
u Elastic strain energy density
U Elastic strain energy
U_V Elastic strain energy of volume of a void
V Volume
w Dislocation channel width
W Work
α Obstacle hardness
β Compressibility, work hardenability
ϕ Neutron flux
Φ Neutron fluence
ϕt_e Effective neutron fluence
Δ Volume strain
δ Increment of distance
ε, ε_{ij} Strain and components of strain
γ Dislocation channel strain
γ_{SFE} Stacking-fault energy
Γ Dislocation line tension
λ Lamé coefficient
μ Shear modulus
ν Poisson's ratio
ρ_d Dislocation density
σ Tensile stress
σ_i Friction stress
σ_m Mean stress

σ_s	Shear stress
σ_s^0	Athermal component of flow stress
σ_y	Yield stress
σ_{yp}	CRP contribution to yield stress
σ_{ypm}	Yield strength plateau
τ	Defect lifetime
ζ	Number of damage zones created per neutron collision

Subscripts

d	Dislocation
f	Fracture
i, j or x, y, z	Stress and strain components
loop	Loops
LR	Long range
n	Necking
ppt	Precipitates
s	Shear or strong
SR	Short range
u	Uniform
void	Voids
V	Void
w	Weak
y	Yield
yr	Root-sum-square
yl	Linear sum

Superscripts

n	Strain hardening exponent

Acronyms

AFM	Atomic-force microscope
APT	Atom probe tomography
CRP	Copper-rich precipitates
MF	Matrix features
RA	Reduction in area
RAH	Radiation anneal hardening
RPV	Reactor pressure vessel
RSS	Root-sum-square
SEM	Scanning electron microscopy
SFE	Stacking-fault energy
SMF	Stable matrix features
TEM	Transmission electron microscope

UMF Unstable matrix features
UTS Ultimatetensile strength
YS Yield strength

Problems

12.1 The irradiated microstructure will determine the extent of hardening in an alloy. Your goal is to limit the radiation hardening in a metal. Assume that all hardening comes from voids and that no transmutation gas is present. For a fixed number of vacancies trapped in cavities, would you prefer a large density of small voids or a small density of large voids? Explain your reasoning.

12.2 If an alloy swells by an increase in the radii of voids at constant density, by how much does a doubling of the swelling harden the alloy? For this scenario, is the swelling or the hardening from voids more of a concern?

12.3 Electron microscopic examination of a 316 stainless steel specimen that has been irradiated at 400 °C in a fast neutron fluence of 1×10^{22} n/cm^2 ($E > 0.1$ MeV) reveals voids with an average diameter of 40 nm and a number density of 2.2×10^{15} cm^{-3}. In addition, faulted loops of a diameter 16 nm are present at a number density of 1.8×10^{15} cm^{-3}. The incremental increase in the shear stress caused by a barrier can be expressed as:

$$\Delta\tau = \alpha\mu b/l\left(\mu = 80\,\text{GPa}, b = 2.5 \times 10^{-10}\,\text{m}\right)$$

Assuming that both types of defects act as hard barriers ($\alpha = 1$ for voids, $\alpha = 1/2$ for faulted loops) and are distributed in regular, square arrays:

(a) Calculate the change in the critical resolved shear stress ($\Delta\tau$) due to irradiation.
(b) What is the interparticle spacing of the square arrays?
(c) Which causes greater hardening, voids, or loops?

12.4 For 316 stainless steel irradiated at 400 °C to a fast neutron fluence of 1×10^{22} n/cm^2 ($E > 0.1$ MeV), determine the dislocation loop size and density required to produce the same hardening as the void population given in Problem 12.3.

12.5 A pressure vessel steel is irradiated at 300 °C to a fluence of 10^{20} n/cm^2. We wish to determine the change in NDT due to such an irradiation. NDT is defined by the condition that $\sigma_f = \sigma_y$ or $\sigma_y k_y = 4\mu\gamma d^{-1/2}$. The effect of irradiation on source hardening can be determined as follows:

$$d\left(\sigma_y k_y\right) = \sigma_y dk_y + k_y d\sigma_y = 0,$$

since the term $4\mu\gamma d^{-1/2}$ is essentially constant during irradiation.

The changes in k_y and σ_y due to the variables T and ϕt (where ϕt is manifest by radiation hardening or an increase in the friction stress σ_i) are given as:

$$dk_y = \frac{\partial k_y}{\partial T} dT + \frac{\partial k_y}{\partial \sigma_i} d\sigma_i$$
$$d\sigma_y = \frac{\partial \sigma_y}{\partial T} dT + \frac{\partial \sigma_y}{\partial \sigma_i} d\sigma_i.$$

Combining these expressions and neglecting the effect of radiation on source hardening ($\partial k_y/\partial \sigma_i = 0$ and $\partial \sigma_y/\partial \sigma_i = 1$), we obtain an increase in transition temperature dT_D;

$$\frac{dT_D}{d\sigma_i} = -\left(\frac{\sigma_y}{k_y}\frac{\partial k_y}{\partial T} + \frac{\partial \sigma_y}{\partial T}\right)^{-1}.$$

To find the increase in transition temperature dT_D as a function of fluence, we need the dependence of friction stress σ_i on ϕt. This will give us:

$$dT_D = \frac{dT_D}{d\sigma_i}\frac{d\sigma_i}{d(\phi t)} d(\phi t).$$

Using Makin's theory for hardening by depleted zones,

$$\sigma_i = \sigma_i^0 [1 - \exp(-\alpha V \Sigma_s \phi t)]^{1/2}$$

and that

$$\sigma_i^0 = 6.64\,\text{GPa}$$
$$\alpha = 1$$
$$\Sigma_s = 0.26\,\text{cm}^{-1}$$

and a cluster size of 6 nm, calculate the increase in transition temperature dT_D after a fluence increment of 10^{20} n/cm^2, given that $dT_D/d\sigma_i \sim 0.3$ °C/MPa.

12.6 The work hardening region of the stress–strain curve can be represented by the relation $\sigma = k\varepsilon^n$, where n is the work hardening coefficient. By increasing the yield stress more than the ultimate tensile stress, irradiation effectively reduces the work hardening coefficient. Using the criterion for plastic instability, $d\sigma/d\varepsilon = \sigma$, calculate the reduction in uniform elongation due to an irradiation that decreases n by an amount Δn.

12.7 A specimen of Ni–1Al is irradiated at 550 °C with 3.5 MeV nickel ions to a dose of 9 dpa. The resulting structure contains a void distribution consisting of 3×10^{14} voids/cm^3 at an average diameter of 50 nm.

(a) What is the required stress for a dislocation to cut through an array of these barriers and what fraction is this of the full Orowan stress?
(b) Assuming a constant total void volume, what is the stress if void growth causes the average void size to double?

Use the elastic constants for pure nickel and assume a grain size of 10 μm.

12.8 Consider a dislocation line in a solid containing N bubbles of radius R per cubic centimeter. A shear stress, τ_{xy}, is applied to the solid, which causes the dislocation to glide along its slip plane. Under what conditions will the bubbles be swept along by the dislocation rather than be bypassed by it?

12.9 You have 3 tensile samples of 316 stainless steel. Two were irradiated in a reactor to 10^{21} n/cm^2 at 300 °C and one was left unirradiated. The three samples are tested in a tensile test in the laboratory in the following manner: One irradiated sample is tested at room temperature, another at 300 °C, and the unirradiated sample is tested at 300 °C, all at the same strain rate. On a single graph, draw the engineering stress–engineering strain curves that would result, labeling the points σ_y, σ_{UTS}, σ_f, ε_u, ε_f. Provide a brief explanation justifying the relative positions of the curves.

12.10 Draw the engineering stress–engineering strain curves that would result from a tensile test in the laboratory on the samples in Problem 12.9 following irradiation to 10^{21} n/cm^2 at 300 °C and 700 °C. Label the points σ_y, σ_{UTS}, σ_f, ε_u, ε_f.

References

1. Dieter GE (1976) Mechanical metallurgy, 2nd edn. McGraw-Hill, New York
2. Kocks UF (1970) Metal Trans 1:1121–1143
3. Olander DR (1976) Fundamental aspects of nuclear reactor fuel elements, Chap 18. TLD-26711-Pl. Technical Information Center, ERDA, Washington, DC
4. Stroh AN (1954) Proc Roy Soc Vol London 223:404–414
5. Makin MJ, Sharp JV (1965) Phys Stat Sol 9:109
6. Singh BN, Foreman AJE, Trinkaus H (1997) J Nucl Mater 249:103–115
7. Stoller RE (2000) SJ Zinkle. J Nucl Mater 283–287:349–352
8. Seeger A (1958) Proceedings of 2nd United Nations international conference on the peaceful uses of atomic energy, Geneva, vol 6. United Nations, NY, p 250
9. Russell KC, Brown LM (1972) Acta Metal 20:969–974
10. Scattergood RO, Bacon DJ (1982) Acta Metal 30:1665–1677
11. Kocks UF, Arbon AS, Ashby MF (1975) Prog Mater Sci 19:1
12. Kocks UF (1977) Mater Sci Eng 27:291–298
13. Bement AL (1972) Rev Roum Phys 17(3):361–380
14. Foreman AJE, Makin MJ (1967) Can J Physics 45:511
15. Kocks UF (1969) Physics of strength and plasticity. MIT Press, Cambridge, p 13
16. Odette GR, Lucas GE (1998) Rad Eff Defects Solid 44:189
17. Lucas GE (1993) J Nucl Mater 206:287–305
18. Was GS, Busby JT, Andresen PL (2006) Corrosion in the Nuclear Power Industry, ASM handbook, vol 13C. ASM International, pp 386–414

19. Was GS, Andresen PL (2007) Effect of irradiation and corrosion on SCC in LWRs, Corrosion in the Nuclear Power Industry, vol 13 B, Chap 5-A3. American Society for Metals, Metals Park, OH (in press)
20. Zinkle SJ, Maziasz PJ, Stoller RE (1993) J Nucl Mater 206:266–286
21. Garner FA (1993) J Nucl Mater 205:98–117
22. Kojima S, Zinkle SJ, Heinisch HL (1989) Grain size effect on radiation hardening in neutron-irradiated polycrystalline copper, fusion reactor materials semiannual progress report for period ending March 31, 1989, DOE/ER-0313/6: 43–49
23. Makin MJ, Minter FJ (1957) J Inst Metals 24:399
24. Higgy HR, Hammad FH (1975) J Nucl Mater 55:177–186
25. Odette GR, Lucas GE (1991) J Nucl Mater 179–181:572–576
26. Bement AL (1963) HW-74955, p 181
27. Eason ED (1998) Development, evaluation and analysis of the initial CIR-IASCC database, EPRI Report TR-108749, Oct 1998, pp 3–7 to 3–10
28. Williams JA, Hunter CW (1972) Effects of radiation on substructure and mechanical properties of metals and alloys, STM STP 529. American Society for Testing and Materials, Philadelphia, PA, p 13
29. Pettersson K (1992) Radiation effects on mechanical properties of light water reactor structural materials, TR1TA-MAC-0461. Materials Research Center, The Royal Institute of Technology, Stockholm
30. Was GS, Busby JT (2003) Use of proton irradiation to determine IASCC mechanisms in light water reactors: solute addition alloys, final report, project EP-P3038/C1434, Report #1007440. Electric Power Research Institute, Palo Alto, CA, April, 2003
31. Garner FA, Hamilton ML, Panayotou NF, Johnson GD (1981) J Nucl Mater 103(104): 803–808
32. Grossbeck ML, Maziasz PJ, Rowcliffe AF (1992) J Nucl Mater 191–194:808–812
33. Zinkle SJ (1992) In: Stoller RE, Kumar AS, Gelles DS (eds) Effects of radiation on materials the 15th international symposium, ASTM STP 1125. American Society for Testing and Materials, Philadelphia, PA, 1992, pp 813–834
34. Bloom EE (1976) Irradiation strengthening and embrittlement. Radiation damage in metals. American Society for Metals, Metals Park, pp 295–329
35. Hashimoto N, Wakai E, Robertson JP (1999) J Nucl Mater 273:95–101
36. Ando M, Katoh Y, Tanigawa H, Kohyama A, Iwai T (2000) J Nucl Mater 283–287:423–427
37. Maziasz PJ (1993) J Nucl Mater 205:118–145
38. Kelly PM (1972) Scr Metal 6:647
39. Odette GR, Lucas GE, Klingensmith RD, Stoller RE (1996) In: Gelles DS, Nanstad RK, Kumar AS, Little EA (eds) Effects of radiation on materials the 17th international symposium, STM STP 1270. American Society for Testing and Materials, Philadelphia, PA, 1996, pp 606–636
40. Odette GR, Mader EV, Lucas GE, Phythian W, English CA (1993) In: Kumar AS, Gelles DS, Nanstad RK, Little EA (eds) Effects of radiation on materials the 16th international symposium, ASTM STP 1175. American Society for Testing and Materials, Philadelphia, PA, 1993, p 373
41. Odette GR, Yamamoto T, Klingensmith D (2005) Phil Mag 85(4–7):779–797
42. Kasada R, Kitao T, Morishita K, Matsui H, Kimura A (2001) In: Rosinski ST, Grossbeck ML, Allen TR, Kumar AS (eds) Effects of radiation on materials the 20th international symposium, ASTM STP 1405. American Society for Testing and Materials, West Conshohocken, PA, 2001, p 237
43. Schaeublin R, Gelles D, Victoria M (2002) J Nucl Mater 307–311:197–202
44. Gupta G, Jiao Z, Ham AN, Busby JT, Was GS (2006) Microstructural evolution of proton irradiated T91. J Nucl Mater 351(1–3):162–173
45. Wechsler MS, Murty KL (1989) Metal Trans A 20A:2637–2649
46. Ohr SM, Tucker RP, Wechsler MS (1970) Phys Status Solidi A 2:559–569

47. McClintock FA, Argon AS (1966) Mechanical metallurgy of materials. Addison-Wesley, New York
48. Tabor D (1956) The physical meaning of indentation and scratch hardness. Brit J App Phy 7:159
49. Prandtl L (1920) Nachr Ges Wiss, Gottingen, p 74
50. Hencky H, Agnew Z (1923) Math Mech 3:250
51. Larsson PL (2001) Investigation of sharp contact at rigid-plastic conditions. Int J Mech Sci 43:895–920
52. Busby JT, Hash MC, Was GS (2005) J Nucl Mater 336:267–278
53. Lucas GE, Odette GR, Maiti R (1987) Sheckherd JW (1987). In: Garner FA, Henagar CH, Igata N (eds) Influence of radiation on materials properties the 13th international symposium (Part II), STM STP 956. American Society for Testing and Materials, Philadelphia, PA, pp 379–394
54. Strudel JL, Washburn J (1964) Phil Mag 9:491
55. Gelles DS (1981) In: Ashby MF, Bullough R, Hartley CS, Hirth JP (eds) Proceedings of dislocation modeling of physical systems. Pergamon, Oxford, p 158
56. Foreman AJE, Sharp JV (1969) Phil Mag 19:931
57. Tanigawa H, Kohyama A, Katoh Y (1996) J Nucl Mater 239:80
58. Eyre BL, Bullough R (1965) Phil Mag 12:31
59. Eyre BL (1962) Phil Mag 7:2107
60. Tucker RP, Wechsler MS, Ohr SM (1969) J Appl Phys 40(1):400–408
61. Byun TS, Farrell K (2004) Acta Mater 52:1597–1608
62. Was GS, Jiao Z, Busby JT (2006) In: Gdoutos EE (ed) Proceedings of the 16th European conference of fracture. Springer, Berlin
63. Byun TS, Hashimoto N (2006) J Nucl Mater 354:123–130
64. Jiao Z, McMurtrey M, Was GS (2011) Scr Mater 65:159–162
65. Jiao Z, Was GS (2010) J Nucl Mater 407:34–43
66. Byun TS, Hashimoto N, Farrell K, Lee EH (2006) J Nucl Mater 354:251–264
67. Frost HJ, Ashby MJ (1982) Deformation-mechanism maps: the plasticity and creep of metals and ceramics. Pergamon, New York
68. Zinkle SJ, Lucas GE (2003) Deformation and fracture mechanisms in irradiated fcc and bcc metals. US Department of Energy, Semi-Annual Report, DOE-ER-0313/34, p 117
69. Byun TS, Hashimoto N, Farrell K (2006) J Nucl Mater 351:303–315
70. Farrell K, Byun TS, Hashimoto N (2004) J Nucl Mater 335:471–486